POLITECNICO DI MILANO
Corso di Laurea Magistrale in Ingegneria Industriale e Dell'Informazione
Dipartimento di Mechanica

High Order Discontinuous Galerkin Simulations of a Rotating Cylinder

Relatore: Professor Luca Bonaventura
Correlatore: Professor Antonella Abbà

Tesi di Laurea di:
Alejandro Valencia, matricola 893798

Anno Accademico 2020-2021

To my mom

Abstract

The topic of this thesis is the application of high order Discontinuous Galerkin methods to flow past a rotating cylinder with harmonic time dependent boundary conditions for Reynolds number 10^2 and 10^3. The methods yield force coefficients that matched well with results reported in literature and vortex shedding synchronization was obtained. Degree adaptivity (or p-adaptivity) was successfully applied to achieve high levels of accuracy only where necessary, saving computational time compared to the constant degree simulations. An error indicator based on the modal coefficients of the momentum was utilized. In addition, a preliminary turbulent simulation at $Re = 5000$ using LES models was carried out to determine whether simulations in a non-inertial reference frame could produce valid statistics. Instabilities were encountered leading to the conclusion that large domains with large solution damping layers are required.

Acknowledgements

I express the upmost gratitude to my advisors Dr. Antonella Abbà and Dr. Luca Bonaventura who gave me, a mechanical engineer, the opportunity to complete a thesis that dove into a topic within the mathematical and aerospace fields. Thank you for always being available to answer any and all questions I had. Most importantly, thank you for motivating me during the times where I struggled. You gave me hope to continue and succeed.

Thank you to the staff at CINECA for the support and patience in dealing with a first time user of a supercomputer. My best wishes to them on their future collaborations and endeavors to solve today's and tomorrow's problems.

A thanks that cannot go unsaid is to all my friends both local and abroad, who's conversations no matter how small, made my day every day. You truly kept me going and taught me to never give up. Special thanks goes to Prasad Rao who became like a brother, talking, having fun, and creating priceless memories on our little adventures around Milan; to Shruthi, who's teatime took me to a place away from university studies and reminded me to pause and enjoy life; to Laura Solari, who made me feel at home in Italy not only by answering my one million questions about the Italian culture and language but also for sending me the countless memes that brought me the biggest of laughs.

Thank you to Gina Farella and Guiseppe Gambardella, my landlords for the majority of my stay in Milan. Gina, you truly made feel like I was part of your family and not just a simple guest. You made sure that I was always comfortable at home providing me with anything I needed. Our Sunday lunches are something I will treasure for a lifetime. Guiseppe, know that wherever you are looking from, you have touched my heart and I will never forget all the kind things you did for me.

The greatest thanks goes to my mom. Without her support and love none of my accomplishments could have come to fruition. You let your only son travel across the continent and an ocean to fulfill his dream of

completing a Master's degree in Europe. You comforted me at my worst moments, and you cheered for me with all your strength. I cannot truly express how grateful I am for everything you have done for me. I strive every day to make you proud. From the bottom of my heart, thank you.

Contents

List of Figures

List of Tables

Chapter 1

Introduction

1.1 General Overview

Many aspects of life consist of fluid motion; from water flowing down rivers to wind blowing across fields. It did not take long before people tried to exploit this flow for personal use. River and windmills began to appear around the world, converting the natural motion of water or air to do work. A new branch of Physics was soon created with the aim to scientifically model these motions through complex equations.

Fluid Mechanics, the name given to this branch of Physics, is founded on the continuum hypothesis. This hypothesis states that the fluid can be modeled as a continuous medium rather than by individual molecules. Properties such as density and pressure are defined at minute length scales that are still larger than the molecular ones. This assumption has proven to be accurate in many cases and is thus utilized in scientific practice.

Fluid flow can be further categorized by whether viscous or inertial forces dominate. When the viscous forces are dominant, the fluid tends to be calm and follow smooth streamlines. Injecting color dye into the flow, the fluid would spread or diffuse the ink throughout the domain. This case is known as laminar flow. The latter case when inertial forces are dominant is known as turbulence. The fluid motion is no longer predictable as chaotic motion and heavy mixing is present. Now if color dye is injected, the ink will be transported or convected along curved and three dimensional streamlines.

When the continuum hypothesis is adopted, turbulence cannot be ignored. Fortunately, the equations that govern fluid flow are the same for both cases. The difficulties lie, instead, in the capture of the wide range of length and time scales turbulence exhibits. The swirling motion of the fluid form vortices that in time, breakdown into smaller and smaller structures

until the smallest scales dissipate the remaining kinetic energy.

Since the behavior of the fluid is highly dependent on whether viscous or inertial forces are dominant, a non-dimensional ratio was developed by Osborne Reynolds (1842-1912) to determine in which region the flow is in. This ratio is given by

$$Re = \frac{\rho V_r L}{\mu}, \tag{1.1}$$

where ρ is the density of the fluid, L is the characteristic length of the considered problem, V_r is a reference velocity, and μ is the dynamic viscosity of the fluid. Larger values of Re indicates that the flow under consideration is in the turbulent regime i.e., convection dominates diffusion.

Although not present in the Reynolds number, it is important to note the significant role of the temperature of the fluid. Indeed, the viscosity is not a constant property of the fluid, since the energy brought by the heat exchange reduces the intermolecular forces that keep a liquid together. The opposite occurs with gases. As the temperature rises, particles that are more spaced out interact with regions of higher density. Momentum is transferred causing a resistance to motion and increasing the effective viscosity.

The fluid flow equations, now named the Navier-Stokes equations after the extensive works of Claude-Louis Navier (1785-1836) and George Gabriel Stokes (1819-1903), only admit closed form, analytic solutions in a few cases. Thus, physicists and engineers turned to Computational Fluid Dynamics (CFD). CFD is the application of numerical methods to these equations allowing to simulate phenomenon that would otherwise be infeasible to describe correctly due to complexity or cost. As computers become more powerful and new efficient mathematical models are developed, CFD simulations will continue to increase in accuracy, solidifying its importance in the design process.

At the crux of CFD, the domain is discretized into many smaller ones to capture all the physics that is present in a flow case. The resolution of the computational grid therefore must be high to ensure this requirement. For simulations of turbulent flows, the size of the discrete domains becomes more and more important as the vortex structure range becomes larger. The smallest vortices continue to heavily influence the flow at high values of Re. Laminar flow simulations on the other hand, can be accurate with a coarse grid resolution. However, flow profiles can be nonlinear and there must be an adequate number of discrete points to model the flow correctly.

Simulations where the grid is discretized to such a degree that all the physics of the flow are properly captured, are known as Direct Numerical

Simulations (DNS). The computational time required by DNS can be extremely large, since achieving such a level of accuracy demands a massive number of degrees of freedom. As a consequence, DNS is reserved for more theoretical test cases where experiments are more costly or difficult to perform.

To make CFD viable in industry, numerical simulations have initially been based on the Reynolds Averaged Navier-Stokes (RANS) equations. Within the RANS framework, the averaged quantities of interest are solved, and any effects of turbulence are modeled by fluctuations. These fluctuations in turn introduce extra terms and equations that are solved via the numerical method chosen. Because RANS simulations model the effect of turbulence, no eddies are physically captured bypassing the necessity for extreme grid resolutions. The computational time for RANS simulations are orders of magnitude smaller than DNS but at the cost of accuracy. Nevertheless, RANS continues to be the most common method to solve turbulent flow problems in industrial practice.

An intermediate approach is known as Large Eddy Simulation (LES). LES aims to solve directly the largest eddies caused by turbulence and model only the smallest ones. This filtering technique avoids the additional equations introduced in RANS based simulations. Moreover, this approach is favorable since according to Kolmogorov, the smallest scales at sufficiently high Reynolds numbers are isotropic, thus, simple models can be employed [36]. Starting with the work of researchers such as Smagorinsky [54] and Lilly [37], LES has been studied and found to provide comparable results to DNS while taking significantly less computational time. In addition, current computing power and parallelism has made LES more practical and desirable.

Despite modern computer advancements, LES is still out of reach for many industrial simulations, not only because the grid resolution is higher than RANS simulations, but the filtering operation is nontrivial on unstructured meshes [66]. The filter size is not known *a prioi* and the type of filter can influence the solution to the numerical problem. The filtering can be explicit with uniform width, perfectly suitable for simple cases such as homogenous isotropic turbulence or plane channel flow (examples in [22] and [51]). For more complex situations, implicit filtering is employed. The Navier-Stokes equations are now discretized on the computational grid itself. When the grid is non-uniform and unstructured, the filter definition also loses its uniformity. It is therefore difficult to use standard error estimation tools especially when the different sized local domains offer unique filter lengths [49]. The estimation of the proper filter can lead to regions of

insufficient or excessive refinements. Most choices regarding the resolution must rely on similar case studies.

1.2 Numerical Approximation

The Navier-Stokes equations are functions of time and space and thus require approximating the solution in both physical dimensions. While most time integration methods are based on those applied to systems of Ordinary Differential Equations, there is a much greater variety of spatial discretization approaches. The Finite Volume Method (FVM) is most often seen in industry for its ability to be applied to arbitrary geometries and its preservation of mass. For the work presented, a Discontinuous Galerkin (DG) Finite Element (FE) numerical framework is employed. The DG method has the ability to be used on an unstructured grid and the possibility to achieve high degrees of accuracy by increasing the order of the polynomial basis. In addition, the presence of finite volume face fluxes couples elements together, ensuring the conservation of mass is satisfied. The DG method is a candidate to replace the Finite Volume Method (FVM) with its potential for parallelization and the growing trend in higher core counts in current computer processors. Moreover, the low dissipation aspect of the DG method makes it particularly interesting for researching under-resolved turbulence cases [13].

1.3 Outline of Thesis

The focus of this thesis is on the simulations of flow past a rotating cylinder. The fluid dynamics of uniform flow past a stationary cylinder are well understood and have been studied for many years, making it a good benchmark for theoretical, experimental, and numerical tests. Many attempts have been made to further the scientific understanding of the effects rotation has on this type of flow configuration. A basic schematic of the problem studied is shown in Figure 1.1.

The Reynolds number for this scenario can be expressed by Equation 1.2, where $\nu = \rho/\mu$ is the kinematic viscosity, D is the cylinder diameter, and U_∞ is the freestream (or translating) velocity:

$$Re = \frac{U_\infty D}{\nu}. \tag{1.2}$$

For a stationary cylinder, a wake develops, and at a certain Reynolds number (around 47 [43]), vortices can be shed with a specific frequency.

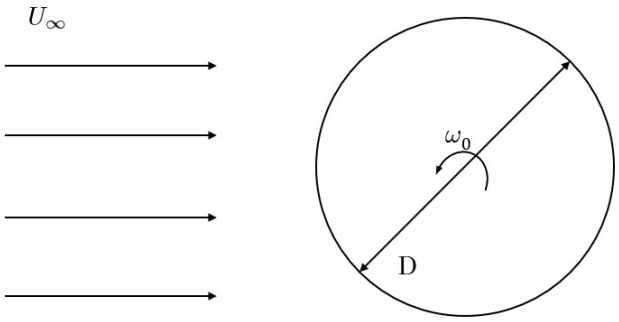

Figure 1.1: Rotating Cylinder

This frequency is unique and if nondimensionalized is known as the Strouhal number:

$$St = \frac{f_{vs}D}{U_\infty}. \tag{1.3}$$

f_{vs} is the vortex shedding frequency, found by analyzing the oscillations in the lift force. As the trailing vortices are shed, they generate a lift force with a zero mean value. The drag force, on the other hand, oscillates at a frequency twice this value.

It is also well understood that, if instead the cylinder rotates, the fluid on either the upper or lower surface will accelerate and the flow on the opposite side will decelerate. This change in momentum causes an increase in the mean value of the lift force that is also known as the Magnus effect. This effect is described in greater detail by Prandtl in [44] and in a modern context by Seifert in [53].

Prandtl first theoretically postulated that a maximum lift coefficient could be achieved equal to 4π in uniform flow. He stressed the importance of the non-dimensional rotation rate, α, on the physics of the problem. It is defined as the ratio between the tangential velocity at the cylinder's edge, U_T, and the freestream velocity:

$$\alpha = \frac{U_T}{U_\infty}. \tag{1.4}$$

A rather curious phenomenon, theorized by Glauert in 1957, is that at critical values of α, vortex shedding in the cylinder wake could be suppressed [33]. This led to the experiments performed by Coutanceau and Menard in 1985 [21], Badr *et al* in 1990 [8], and Tokumaru *et al* in [58]. These experiments validated the hypothesis that vortex shedding did in fact

cease at certain values of α. However, these results documented the significant role the Reynolds number has in the flow development. Tokumaru's experiments in particular also proved that at high enough values of the non-dimensional rotation rate (specifically $\alpha > 5$), the maximum lift coefficient exceeds Prandtl's limit [58]. In addition, at lower rotation rates, higher values of lift were reported.

Numerical studies have been performed in [8], [12], [15], [17], and [41] in the laminar regime ($Re = 200$ and 1000), varying the non-dimensional rotation rate. Each of these papers takes on a different approach achieving successful results compared to the reference data. In addition to an increase in the lift force, a significant reduction in drag was observed.

Note that all of the previous references researched cases where the rotational speed was constant. In this work, simulations were also conducted where α was subjected to a harmonic forcing.

Taneda in [56], experimentally observed that rotary oscillation could also be a means to suppress vortex shedding. The experiments were carried out in the laminar regime with the Reynolds number ranging from 30 to 300. The idea that the rotation rate could control the cylinder wake interested researchers Tokumaru and Dimotakis, leading to their experiments in [57] for a turbulent case where $Re = 15000$. Not only did they find that vortex shedding ceased, but also that the drag force was significantly reduced compared to a stationary cylinder.

On the numerical side, Lu and Sato in [39] investigated the same test case as Taneda at α ranging from 0.1 to 3 and $Re = 200$, 1000, and 3000, varying the ratio between rotary oscillation and vortex shedding frequency. They found that for certain rotation rates the frequency of vortex shedding could be synchronized to the forcing one. This phenomenon is quite interesting as it allows for the possibility of direct control of the cylinder wake. Because the lift force is not constant but oscillatory, the vibrations can cause structural damage if their frequency is near resonance.

This thesis applies the adaptive DG method described in [61], [60], and [46] to the numerical simulation of flow past a rotating cylinder in two dimensions. In addition, some results of a 3D test case are presented, computed in a non-inertial reference frame. It was found that this approach led to numerical difficulties that will be explained in Chapter 5. More specifically, this thesis is organized as follows.

2. Governing Equations: In this chapter, the Navier-Stokes Equations in a non inertial reference frame are derived. Moreover, they are nondimensionalized in order to make comparable results to literature.

3. LES Formulation: The concept of filtering the Navier-Stokes Equations is explored. Three subgrid scale LES models are detailed.

4. Space and Time Discretization: Here, the Discontinuous Galerkin Method is introduced at a elementary level. Specifically, the Local Discontinuous Galerkin Method will be discussed. Degree adaptivity is explained along with a brief overview on the time discretization.

5. Results: Force statistics are computed and compared to the reference. The flow quantities are plotted to visualize the wake formation. A frequency analysis is carried out to isolate the Strouhal number of the shedding vortices.

6. Concluding Remarks: Final comments are made about the results and potential future work.

Chapter 2

Governing Equations

2.1 Navier-Stokes Equations

The compressible Navier-Stokes equations are shown below, written in an inertial reference frame. The indices i and j represent the Cartesian coordinates (for 2 dimensions i and j will be replaced with x and y):

$$\frac{\partial \rho^d}{\partial t^d} + \frac{\partial (\rho^d u_j^d)}{\partial j} = 0, \tag{2.1a}$$

$$\frac{\partial (\rho^d u_i^d)}{\partial t^d} + \frac{\partial (\rho^d u_i^d u_j^d)}{\partial j} + \frac{\partial p^d}{\partial i} - \frac{\partial \sigma_{ij}^d}{\partial j} = \rho^d f_i^d, \tag{2.1b}$$

$$\frac{\partial (\rho^d e^d)}{\partial t^d} + \frac{\partial (\rho^d h^d u_j^d)}{\partial j} - \frac{\partial (\sigma_{ij}^d u_i^d)}{\partial j} + \frac{\partial q_j^d}{\partial j} = \rho^d f_j^d u_j^d \tag{2.1c}$$

These equations express the conservation of mass, momentum, and energy applied to a differential element of fluid, respectively. To close the above system the equation of state for an ideal gas is introduced:

$$\frac{p^d}{\rho^d} = RT^d. \tag{2.2}$$

Note that the superscript d signifies dimensional terms.

2.2 Navier-Stokes Equations in a Non-Inertial Reference Frame

Recall the purpose of this work was to study the turbulent fluid flow in a non-inertial reference frame. It will be discussed later why this approach

was abandoned for the 2D simulations but, the concept is nevertheless quite interesting and was used for the turbulent test cases. The following section is included to introduce the equations necessary to simulate such a type of flow configuration.

To avoid using rotating grids or time dependent boundary conditions, the quantities in Equation (2.1) are written in the rotating reference frame directly. This leads to the advantage of maintaining the same form of the equations while only modifying the forcing term with additional components.

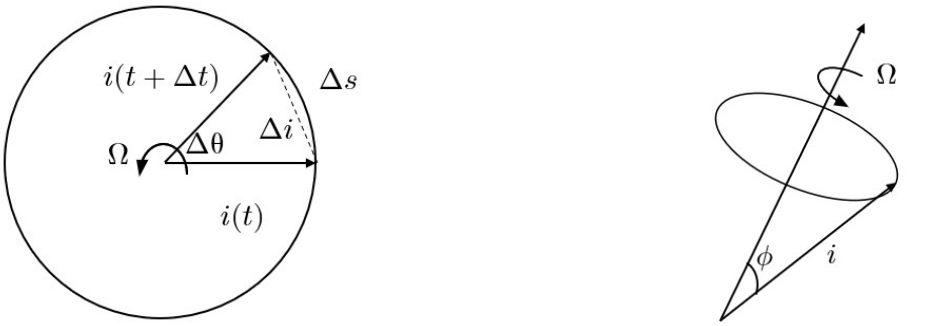

(a) Unit vector perpendicular to rotation

(b) An offset rotating unit vector

Figure 2.1: A Rotating Unit Vector

First, consider a stationary reference frame where a unit vector, $\boldsymbol{i}$, is rotating with an angular velocity, $\boldsymbol{\Omega}$ as depicted in Figure 2.1a. After a small time step, Δt, vector $\boldsymbol{i}$ has both rotated and translated to a new position along a circular path. The arc length between these two positions can be expressed as

$$\Delta s = r\Delta\theta, \tag{2.3}$$

where Δs is the arc length, r is the radius measured from the center of rotation to the tip of vector $\boldsymbol{i}$, and $\Delta\theta$ is the angular displacement which is given by $\Delta\theta = \Omega\Delta t$. If the unit vector lies in the unit circle then (2.3) reduces to

$$\Delta s = \Delta\theta. \tag{2.4}$$

If it does not, then

$$\Delta s = |\boldsymbol{i}| \sin\phi\Delta\theta, \tag{2.5}$$

where ϕ represents the angle from the center of rotation to the unit vector shown in Figure 2.1b.

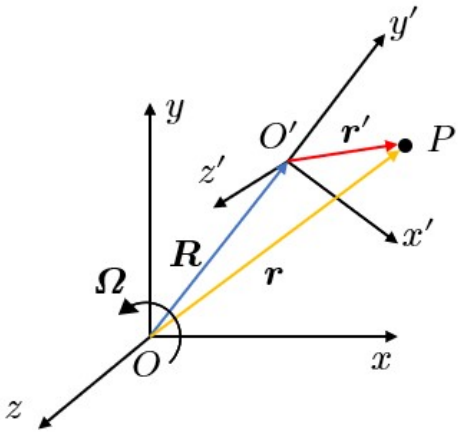

Figure 2.2: A Rotating and Translating Reference Frame

As Δt tends towards zero, it can be seen that the arc length Δs can be better and better approximated by the vectorial difference between $\boldsymbol{i}$ at $t_0 + \Delta t$ and t_0. In addition, this difference, $\Delta \boldsymbol{i}$, becomes more perpendicular to the original vector $\boldsymbol{i}$ while being perpendicular to the rotation vector. Using the relation in (2.5) it can be stated that

$$\Delta \boldsymbol{i} = |\boldsymbol{i}| \sin\phi \Delta\theta \frac{\boldsymbol{\Omega} \times \boldsymbol{i}}{|\boldsymbol{\Omega} \times \boldsymbol{i}|}. \tag{2.6}$$

Notice that the magnitude of the unit vector is one and that $|\boldsymbol{i}|\,\Omega \sin\phi$ is the definition of the magnitude of the cross or vector product between $\boldsymbol{i}$ and $\boldsymbol{\Omega}$. Making this substitution into (2.6) the following is obtained:

$$\Delta \boldsymbol{i} = |\boldsymbol{\Omega} \times \boldsymbol{i}|\, \Delta t \frac{\boldsymbol{\Omega} \times \boldsymbol{i}}{|\boldsymbol{\Omega} \times \boldsymbol{i}|}. \tag{2.7}$$

The change in the unit vector is per unit time is then given as

$$\frac{\Delta \boldsymbol{i}}{\Delta t} = \boldsymbol{\Omega} \times \boldsymbol{i} \tag{2.8}$$

or, in terms of derivatives

$$\frac{d\boldsymbol{i}}{dt} = \boldsymbol{\Omega} \times \boldsymbol{i}. \tag{2.9}$$

Now consider a point P that is represented by the displacement vector, $\boldsymbol{r}'$, in a reference frame that is rotating about an inertial one (Figure 2.2). P can also be described in terms of the inertial reference frame itself by $\boldsymbol{r}$.

$\boldsymbol{R}$ represents the displacement of the rotating frame itself with respect to the inertial one. In summary,

$$\boldsymbol{r} = \boldsymbol{R} + \boldsymbol{r}'. \tag{2.10}$$

From classical mechanics, the velocity is given by the time derivative of the displacement. Thus,

$$\boldsymbol{u} = \frac{d\boldsymbol{r}}{dt} = \frac{d\boldsymbol{R}}{dt} + \frac{d\boldsymbol{r}'}{dt}. \tag{2.11}$$

Note that $\boldsymbol{r}'$ can be expressed in terms of the rotating frame's unit vectors:

$$\boldsymbol{r}' = {r'}_i \boldsymbol{i}'_i, \tag{2.12}$$

where ${r'}_i$ are the component magnitudes in the non-inertial reference frame. Taking the time derivative of (2.12) in (2.11) necessitates the product rule since the rotating frame's unit vectors change in time:

$$\frac{d\boldsymbol{r}'}{dt} = \frac{d{r'}_i}{dt}\boldsymbol{i}'_i + {r'}_i \frac{d\boldsymbol{i}'_i}{dt}. \tag{2.13}$$

Substituting now (2.9) into (2.13):

$$\frac{d\boldsymbol{r}'}{dt} = \frac{d{r'}_i}{dt}\boldsymbol{i}'_i + \boldsymbol{\Omega} \times \boldsymbol{r}'. \tag{2.14}$$

Next, substitute (2.14) into (2.11) and the following is obtained:

$$\boldsymbol{u} = \frac{d\boldsymbol{R}}{dt} + \frac{d{r'}_i}{dt}\boldsymbol{i}'_i + \boldsymbol{\Omega} \times \boldsymbol{r}'. \tag{2.15}$$

The first term describes how the rotating reference frame is translating with respect to the stationary one. This term will be ignored since, in this work, the translation of the non-inertial reference frame is not considered. The second term in (2.15) is simply the velocity of the point P with respect to an observer on the non-inertial reference frame ($\boldsymbol{u}'$). The third component links the two reference frames. Notice that the rotational speed is the same for both observers.

To obtain the acceleration, the time derivative of (2.15) is taken:

$$\boldsymbol{a} = \frac{du}{dt} = \frac{d^2{r'}_i}{dt^2}\boldsymbol{i}'_i + \frac{d\boldsymbol{i}'_i}{dt}\frac{d{r'}_i}{dt} + \frac{d\boldsymbol{\Omega}}{dt} \times \boldsymbol{r}' + \boldsymbol{\Omega} \times \frac{d\boldsymbol{r}'}{dt}. \tag{2.16}$$

Recalling (2.13) and (2.9) once again, allows for the simplification of (2.16) into the following:

$$\boldsymbol{a} = \boldsymbol{a}' + \dot{\boldsymbol{\Omega}} \times \boldsymbol{r}' + 2\boldsymbol{\Omega} \times \boldsymbol{u}' + \boldsymbol{\Omega} \times (\boldsymbol{\Omega} \times \boldsymbol{r}'), \tag{2.17}$$

where $\dot{\boldsymbol{\Omega}}$ is the time derivative of the rotational velocity. The rate of rotation is assumed constant for this work thus, the second term in (2.17) is equal to 0. The first term, on the other hand, is simply the acceleration of the fluid in the rotating reference frame.

The remaining terms are the so called fictious forces. The last term, known as the centrifugal force, is the force "felt" when traveling along a circular path. It acts in the radial direction passing through the axis of rotation. As the rotation rate or location from the center of rotation increases, so does the force.

The third term, $2\boldsymbol{\Omega} \times \boldsymbol{u}'$, is known as the Coriolis acceleration. It is the reason why that from an inertial point of view, one would perceive as traveling in a straight path, appears to travel in a curve from the non-inertial frame. Take note this term is only present when the fluid is traveling in a path with a component perpendicular to the rotation. It is the Coriolis force that is responsible for many phenomena in rotating systems, ranging from fluid dynamic slip within turbomachines to hurricanes.

Now that an expression for the acceleration has been derived, (2.1) can be rewritten in the non-inertial frame. Taking (2.17) and substituting it into (2.1) results in

$$\frac{\partial \rho^d}{\partial t^d} + \frac{\partial (\rho^d u_j'^d)}{\partial j} = 0, \tag{2.18a}$$

$$\frac{\partial (\rho^d u_i'^d)}{\partial t^d} + \rho^d \Big(\dot{\Omega}_i^d \times r_i'^d + 2\Omega_i^d \times u_i'^d + \Omega_i^d \times (\Omega_i^d \times r_i'^d) \Big) + \frac{\partial (\rho^d u_i'^d u_j'^d)}{\partial j} + \frac{\partial p^d}{\partial i} - \frac{\partial \sigma_{ij}^d}{\partial j} = \rho^d f_i^d, \tag{2.18b}$$

$$\frac{\partial (\rho^d e^d)}{\partial t^d} + \frac{\partial (\rho h^d u_j'^d)}{\partial j} - \frac{\partial (\sigma_{ij}^d u_i'^d)}{\partial j} + \frac{\partial q_j^d}{\partial j} = \rho^d f_j^d u_j'^d. \tag{2.18c}$$

The velocity under the gradient and divergence operators can be directly substituted with its non-inertial counterpart. This is because spatial terms are invariant with respect to the frame of reference. The same can be said about scalars. Thus, the pressure and density do not require any alterations.

It is common practice to move the additional accelerations in (2.18) and (2.18c) on the right hand side, consolidating all the forces into one term. $\boldsymbol{f}$ now contains the following components:

$$\boldsymbol{f} = \boldsymbol{F}_1 + \boldsymbol{F}_2 + \boldsymbol{F}_3, \tag{2.19}$$

where

$$\boldsymbol{F}_1 = \dot{\boldsymbol{\Omega}} \times \boldsymbol{r}', \tag{2.20a}$$

$$\boldsymbol{F}_2 = 2\boldsymbol{\Omega} \times \boldsymbol{u}', \tag{2.20b}$$

$$\boldsymbol{F}_3 = \boldsymbol{\Omega} \times (\boldsymbol{\Omega} \times \boldsymbol{r}'). \tag{2.20c}$$

2.3 Non-Dimensional Navier-Stokes Equations

It is common practice to nondimensionalize equations to isolate terms that describe or drive the physics of the problem. It allows for the parameterization of the equations by setting a reference value or set of values and introducing new ratios.

To obtain the Navier-Stokes equations in non-dimensional form, reference values for length, density, velocity, temperature, and viscosity, are set. The dimensional terms that appear in Equation (2.1) can be related to the reference values through the following

$$\rho = \frac{\rho^d}{\rho_r}, \qquad \boldsymbol{u} = \frac{\boldsymbol{u}^d}{V_r}, \qquad p = \frac{p^d}{p_r}, \qquad T = \frac{T^d}{T_r}, \tag{2.21a}$$

where the subscript r denotes a reference value.

Lastly, a non-dimensional time is introduced:

$$t = \frac{t^d V_r}{L_r}. \tag{2.22}$$

Rearranging (2.1), the non-dimensional compressible Navier-Stokes equations are given below in vectorial form:

$$\frac{\partial \rho}{\partial t} + \frac{\partial (\rho u_j)}{\partial j} = 0, \tag{2.23a}$$

$$\frac{\partial (\rho u_i)}{\partial t} + \frac{\partial (\rho u_i u_j)}{\partial j} + \frac{1}{\gamma Ma^2}\frac{\partial p}{\partial i} - \frac{1}{Re}\frac{\partial (\sigma_{ij})}{\partial j} = \rho f_i, \tag{2.23b}$$

$$\frac{\partial (\rho e)}{\partial t} + \frac{\partial (\rho h u_j)}{\partial j} - \frac{\gamma Ma^2}{Re}\frac{\partial (\sigma_{ij} u_i)}{\partial j} + \frac{1}{kRePr}\frac{\partial q_j}{\partial j} = \gamma Ma^2 \rho f_j u_j, \tag{2.23c}$$

where the conserved variables are density, ρ, momentum, $\rho\boldsymbol{u}$, and volume specific total energy, ρe.

A powerful non-dimensional term previously discussed is the Reynolds number. This number compares the inertial forces to the viscous ones. As the Reynolds number increases, the flow becomes more and more chaotic as the non-linear terms in the Navier-Stokes equations dominate. Only when Re is low (much less than unity [42]) convective terms can be neglected.

Another important non-dimensional number present in Equation (2.23) is the Mach number. It relates the reference velocity to the speed of sound for that specific fluid. The Mach number is an indicator of how compressibility affects the flow:

$$Re = \frac{\rho_r V_r L_r}{\mu_r}, \tag{2.24}$$

$$Ma = \frac{V_r}{\sqrt{\gamma R T_r}}, \tag{2.25}$$

where R is the ideal gas constant.

In equations (2.1), γ and κ are functions of the gas' specific heats:

$$\gamma = \frac{c_p}{c_v}, \qquad \kappa = \frac{R}{c_p}. \tag{2.26}$$

The remaining quantities in (2.23) are the pressure, p, prescribed forcing, $\boldsymbol{f}$, specific enthalpy, $\rho h = \rho e + p$, and the pair of diffusive fluxes; momentum, σ, and heat, q.

To fully close the system, the non-dimensional ideal gas equation of state is required:

$$p = \rho T, \tag{2.27}$$

where T is the non-dimensional temperature. The total energy can be expressed in terms of the internal one:

$$e_i = \frac{1-\kappa}{\kappa}, \qquad e = e_i + \frac{\gamma M a^2}{2} u_k u_k. \tag{2.28}$$

The diffusive fluxes can be further broken down into the following useful expressions:

$$\sigma_{ij} = \mu \mathcal{S}^d_{ij}, \tag{2.29}$$

$$q_i = -\mu \frac{\partial T}{\partial i}. \tag{2.30}$$

The strain rate tensor is defined as

$$\mathcal{S}_{ij} = \frac{\partial u_i}{\partial j} + \frac{\partial u_j}{\partial i}, \qquad \mathcal{S}^d_{ij} = \mathcal{S}_{ij} - \frac{1}{3}\mathcal{S}_{kk}\delta_{ij}, \tag{2.31}$$

and the dynamic viscosity abides by the power law:

$$\mu\left(T\right) = T^{\alpha}, \tag{2.32}$$

with α set to 0.7.

2.4 Force Coefficients

A fluid when deflected by an obstacle will exert a force on the boundary. This force is caused by normal stresses from the fluid pressure, p, and wall shear stresses from the viscous forces, τ_w. The summation of these components along the surface, Γ, projected onto the direction of the flow, is known as drag. The expression is given by

$$D = \int_{\Gamma} p\cos\left(\theta\right)dA + \int_{\Gamma} \tau_w \sin\left(\theta\right)dA, \tag{2.33}$$

where θ is the angle between the normal vector on the differential boundary element dA, and the flow direction.

The resultant force projected on a direction perpendicular to the direction of the flow, is known as the lift force:

$$L = \int_{\Gamma} -p\sin\left(\theta\right)dA + \int_{\Gamma} \tau_w \cos\left(\theta\right)dA. \tag{2.34}$$

The stress distribution along the surface is typically not known theoretically and can be difficult to measure experimentally. Instead, scientists turn to a more simplified approach, calculating non-dimensional values. These values are the drag and lift coefficients, given by

$$C_d = \frac{D}{\frac{1}{2}\rho U_{\infty}^2 A}, \tag{2.35}$$

$$C_l = \frac{L}{\frac{1}{2}\rho U_{\infty}^2 A}, \tag{2.36}$$

U_{∞} is the freestream or oncoming velocity and A is the reference area. The reference area is arbitrary but in practice and for this thesis work it is taken as the frontal area. The frontal area is the projection of the object seen by an observer from a direction parallel to U_{∞} [42]. For a cylinder in 3

dimensions, the reference area will be given by the diameter multiplied by the span. In 2D it is taken simply as the diameter.

Numerically, the pressure is solved on the points of the grid along the cylinder's surface. The shear stress, for Newtonian fluids, is proportional to the velocity gradient. A discrete integration is performed to obtain the drag and lift forces then their corresponding coefficients are calculated using Equations (2.35) and (2.36).

These force coefficients need to be modified when solving the Navier-Stokes equations in a rotating reference frame. Since the drag and lift are projected onto a direction that is moving with respect to the fixed frame of reference, they require a transformation to determine the true value. This can be done through a multiplication between a rotation matrix and the drag and lift components in the non-inertial reference frame:

$$\begin{bmatrix} C_d \\ C_l \end{bmatrix} = \begin{bmatrix} \cos(\beta) & \sin(\beta) \\ -\sin(\beta) & \cos(\beta) \end{bmatrix} \begin{bmatrix} C'_d \\ C'_l \end{bmatrix}. \tag{2.37}$$

β is given by Ωt or, if the rotation is not constant, $\int \Omega(t)dt$.

Chapter 3

LES Formulation

Recall from the introduction there are a variety of ways to simulate turbulence. This thesis will focus on LES. At a fundamental level, LES aims to reproduce the effect of small eddies not resolved by the computational grid. The most popular LES models are based on the eddy viscosity hypothesis which states energy from large scales dissipate to the smaller ones. More sophisticated models are able to replicate backscatter where smaller eddies have the capability to transfer energy to larger ones. This last point is crucial in simulating any kind of mixing phenomenon.

This chapter opens with the general concept of filtering behind LES then discusses the individual turbulence models with their advantages and disadvantages in detail. Three LES models are chosen for discussion: the Smagorinsky, Dynamic, and Anisotropic models.

3.1 Filtering Technique

At its core, LES takes on the approach to filter the Navier-Stokes equations rather than average them in a turbulent regime thereby resolving only a certain percentage of the eddies. The filter is a spatial one denoted by $\overline{\cdot}$ when applied. The filter length itself is given by $\overline{\Delta}$ and is not arbitrarily set but dependent on the numerical discretization. The filter operation mathematically must conserve constants, be linear, and commute with differential operators. The last requirement is usually not true for finite element discretizations but, the error is assumed small and ignored.

In variable density flows, it is customary to apply the Favre or density weighted average filter to the terms multiplied by the density (denoted by $\widetilde{\cdot}$). This avoids the presence of extra terms arising from combinations between the density ($\rho u, \rho e$, etc.) causing non-closure of the filtered Navier-Stokes

equations [65]. Approximations for these terms become ever increasing difficult to construct with the non-linear combinations such as, ρuu. The Favre filter essentially removes the effect of the density fluctuations by solving per unit volume quantities and reducing the additional terms that require a model.

The Favre filter can be defined for a generic quantity φ as

$$\widetilde{\varphi} = \frac{\overline{\rho\varphi}}{\overline{\rho}}. \tag{3.1}$$

Notice when the Favre filtered quantity is multiplied by the LES filtered density, the original non-linear LES filtered quantity is obtained. The filtered terms multiplied by only the density in (2.23) then become:

$$\overline{\rho u_i} = \overline{\rho}\widetilde{u}_i, \tag{3.2a}$$
$$\overline{\rho e} = \overline{\rho}\widetilde{e}, \tag{3.2b}$$
$$\overline{\rho e_i} = \overline{\rho}\widetilde{e}_i, \tag{3.2c}$$
$$\overline{\rho h} = \overline{\rho}\widetilde{h} = \overline{\rho}\widetilde{e} + \overline{p}. \tag{3.2d}$$

However, when non-linear terms are multiplied by the density, a straightforward substitution between $\bar{\cdot}$ and $\widetilde{\cdot}$ cannot be made, i.e., $\overline{\rho u_i u_j} \neq \overline{\rho}\widetilde{u}_i\widetilde{u}_j$. This is because the term on the left hand side requires knowledge of the unfiltered velocity field. Because the velocity is multiplied by itself, interactions between small and large scales cannot be separated. In order to proceed, a remainder is defined by subtracting the Favre filtered quantities from the LES ones:

$$\varepsilon = \overline{u} - \widetilde{u}. \tag{3.3}$$

Solving for the Favre filtered terms and substituting them into (2.18) the LES filtered Navier-Stokes equations are obtained:

$$\frac{\partial \overline{\rho}}{\partial t} + \frac{\partial(\overline{\rho}\widetilde{u}_j)}{\partial j} = 0, \tag{3.4a}$$

$$\frac{\partial(\overline{\rho}\widetilde{u}_i)}{\partial t} + \frac{\partial(\overline{\rho}\widetilde{u}_i\widetilde{u}_j)}{\partial j} + \frac{1}{\gamma Ma^2}\frac{\partial \overline{p}}{\partial i} - \frac{1}{Re}\frac{\partial \widetilde{\sigma}_{ij}}{\partial j} = -\frac{\partial \tau_{ij}}{\partial j} - \frac{\partial \epsilon_{ij}^{SGS}}{\partial j} + \overline{\rho} f_i, \tag{3.4b}$$

$$\frac{\partial(\overline{\rho}\widetilde{e})}{\partial t} + \frac{\partial(\widetilde{\rho h}\widetilde{u}_j)}{\partial j} - \frac{\gamma Ma^2}{Re}\frac{\partial(\widetilde{u}_i\widetilde{\sigma}_{ij})}{\partial j} + \frac{1}{kRePr}\frac{\partial \widetilde{q}_j}{\partial j} = -\frac{\partial(\rho h u_j)^{SGS}}{\partial j} + \frac{\gamma Ma^2}{Re}\frac{\partial \phi_j^{SGS}}{\partial j} - \frac{1}{\kappa RePr}\frac{\partial \theta_j^{SGS}}{\partial j} + \gamma Ma^2 \overline{\rho} f_j \widetilde{u}_j. \tag{3.4c}$$

Additional steps are taken with the total energy since it is dependent on the velocity, temperature, and internal energy. These quantities must be filtered before the substitution. The relevant expressions are shown below:

$$\overline{\rho}\widetilde{e}_i = \frac{1-\kappa}{\kappa}\overline{\rho}\widetilde{T}, \tag{3.5}$$

$$\overline{\rho}\widetilde{e} = \overline{\rho}\widetilde{e}_i + \frac{\gamma Ma^2}{2}(\overline{\rho}\widetilde{u}_k\widetilde{u}_k + \tau_{kk}). \tag{3.6}$$

Recall that temperature also affects the viscosity. As a direct consequence, the viscous stress tensor and heat flux terms are filtered:

$$\widetilde{\sigma}_{ij} = \mu(\widetilde{T})\widetilde{\mathcal{S}}_{ij}^d, \qquad \widetilde{q}_i = -\mu(\widetilde{T})\frac{\partial \widetilde{T}}{\partial i}, \tag{3.7}$$

where the strain rate tensor along with its deviatoric part is given by

$$\widetilde{\mathcal{S}}_{ij} = \frac{\partial \widetilde{u}_i}{\partial j} + \frac{\partial \widetilde{u}_j}{\partial i}, \tag{3.8}$$

$$\widetilde{\mathcal{S}}_{ij}^d = \widetilde{\mathcal{S}}_{ij} - \frac{1}{3}\widetilde{\mathcal{S}}_{kk}\delta_{ij}. \tag{3.9}$$

Regarding $\boldsymbol{f}$ whenever present, it is considered to be uniform in space and does not generate any concerns when the LES filter is applied.

To close the system the non-dimensional equation of state for ideal gases is also filtered:

$$\overline{\rho T} = \overline{\rho}\widetilde{T} = \overline{p}. \tag{3.10}$$

In (3.4), new terms with the superscript, SGS, are known as subgrid scale terms. They refer to the remainder discussed previously and expressed by (3.3). The main subgrid term of interest is the subgrid stress tensor, τ, given by

$$\tau_{ij} = \overline{\rho u u} - \overline{\rho}\widetilde{u}_i\widetilde{u}_j. \tag{3.11}$$

The other terms are expressed as follows:

$$\begin{aligned} \epsilon_{ij}^{SGS} &= \overline{\sigma}_{ij} - \widetilde{\sigma}_{ij}, & (\rho h u)^{SGS} &= \overline{\rho h u_i} - \overline{\rho}\widetilde{h}\widetilde{u}_i, \\ \phi_j^{SGS} &= \overline{u_i\sigma_{ij}} - \widetilde{u}_i\widetilde{\sigma}_i j, & \theta_i^{SGS} &= \overline{q} - \widetilde{q}_i. \end{aligned} \tag{3.12}$$

These quantities are responsible for the effect small scales exhibit on the larger ones. Since the smallest scales are not resolved the SGS terms require modeling. Whichever model chosen, the small scales should depend on information from the larger ones.

Thanks to efforts of Martín and Vreman ([40], [64]), it was found that $\overline{\sigma}_{ij} \approx \widetilde{\sigma}_{ij}$ and $\overline{q}_i \approx \widetilde{q}_i$ causing the terms ϵ^{SGS}, θ^{SGS}, and ϕ^{SGS} to be negligible.

The fluid's enthalpy can be written in terms of Favre filtered quantities:

$$\begin{aligned} \rho h &= \frac{1}{\kappa}\rho T + \frac{\gamma Ma^2}{2}\rho u_k u_k, \\ \overline{\rho}\widetilde{h} &= \frac{1}{\kappa}\overline{\rho}\widetilde{T} + \frac{\gamma Ma^2}{2}(\overline{\rho}\widetilde{u}_k\widetilde{u}_k + \tau_{kk}). \end{aligned} \tag{3.13}$$

Now the subgrid enthalpy term can be re-expressed as the following:

$$(\rho h u_i)^{SGS} = \frac{1}{\kappa}\mathcal{Q}_i^{SGS} + \frac{\gamma Ma^2}{2}(\mathcal{J}_i^{SGS} - \tau_{kk}\widetilde{u}_i), \tag{3.14}$$

where

$$\mathcal{Q}_i^{SGS} = \overline{\rho u_i T} - \overline{\rho}\widetilde{u}_i\widetilde{T} = \overline{\rho}(\widetilde{u_i T} - \widetilde{u}_i\widetilde{T}), \tag{3.15}$$

$$\mathcal{J}_i^{SGS} = \overline{\rho u_i u_k u_k} - \overline{\rho}\widetilde{u}_i\widetilde{u}_k\widetilde{u}_k = \overline{\rho}\widetilde{u_i u_k u_k} - \overline{\rho}\widetilde{u}_i\widetilde{u}_k\widetilde{u}_k. \tag{3.16}$$

Germano in [27] provided another clever way of expressing (3.16) by introducing generalized central moments:

$$\tau(u_i, u_j, u_k) = \overline{\rho}\widetilde{u_i u_j u_k} - \widetilde{u}_i\tau_{jk} - \widetilde{u}_j\tau_{ik} - \widetilde{u}_k\tau_{ij} - \overline{\rho}\widetilde{u}_i\widetilde{u}_j\widetilde{u}_k. \tag{3.17}$$

With some algebraic manipulation the turbulent diffusion flux can be written as

$$\mathcal{J}^{SGS} = \tau(u_i, u_k, u_k) + 2\widetilde{u}_k\tau_{ik} + \widetilde{u}_i\tau_{kk}. \tag{3.18}$$

Finally, substituting all the previous expressions, the non-dimensional, filtered, Navier-Stokes equations are obtained:

$$\frac{\partial\overline{\rho}}{\partial t} + \frac{\partial(\overline{\rho}\widetilde{u}_j)}{\partial j} = 0, \tag{3.19a}$$

$$\frac{\partial(\overline{\rho}\widetilde{u}_i)}{\partial t} + \frac{\partial(\rho\widetilde{u}_i\widetilde{u}_j)}{\partial j} + \frac{1}{\gamma Ma^2}\frac{\partial\overline{p}}{\partial i} - \frac{1}{Re}\frac{\partial\widetilde{\sigma}_{ij}}{\partial j} = -\frac{\partial\tau_{ij}}{\partial j} + \overline{\rho}f_i, \tag{3.19b}$$

$$\frac{\partial(\overline{\rho}\widetilde{e})}{\partial t} + \frac{\partial(\overline{\rho}\widetilde{h}\widetilde{u}_j)}{\partial j} - \frac{\gamma Ma^2}{Re}\frac{\partial(\widetilde{u}_i\widetilde{\sigma}_{ij})}{\partial j} + \frac{1}{\kappa RePr}\frac{\partial q_j}{\partial j} = -\frac{1}{\kappa}\frac{\partial\mathcal{Q}_j^{SGS}}{\partial j} - \frac{\gamma Ma^2}{2}\frac{\partial(\mathcal{J}_j^{SGS} - \tau_{kk}\widetilde{u}_j)}{\partial j} + \gamma Ma^2\overline{\rho}f_j\widetilde{u}_j. \tag{3.19c}$$

Moving forward, various models will be explored to create an expression for τ_{ij}, $\mathcal{Q}_j^{SGS}$, and $\mathcal{J}_j^{SGS}$

3.2 The Smagorinsky Model

One of most common LES subgrid models was developed by Joseph Smagorinsky in [54]. The Smagorinsky model is based on the eddy viscosity hypothesis first proposed by Boussinesq in 1877 [10]: the idea that turbulence adds to the viscosity as the momentum transfer between vortices dissipates energy. This hypothesis essentially requires the subgrid stress tensor to be aligned or, proportional, with the traceless mean strain rate tensor [50]. The exact relation is shown below:

$$\tau_{ij} - \frac{1}{3}\tau_{kk}\delta_{ij} = -\overline{\rho}\nu^{SGS}\widetilde{\mathcal{S}}_{ij}^d. \tag{3.20}$$

Notice the algebraic characteristic of (3.20). Because no explicit modeling of turbulent fluctuations is necessary, unlike in RANS, no other transport equations are introduced and the calculations in LES become simpler. As pointed out earlier in this text, Kolmogorov determined that the smallest scales are rather isotropic and thus can be modeled in a universal way [36]. The subgrid scale viscosity is expressed by

$$\nu^{SGS} = C_s^2 \overline{\Delta}^2 \left|\widetilde{\mathcal{S}}\right| f_d, \tag{3.21}$$

where the filtered strain rate tensor norm is given by $\left|\widetilde{\mathcal{S}}\right|^2 = \frac{1}{2}\widetilde{\mathcal{S}}_{ij}\widetilde{\mathcal{S}}_{ij}$, $\overline{\Delta}$ is the LES filter length scale, and C_s is the Smagorinsky constant taken to be constant and uniform in the domain. Typically, the Smagorinsky constant is set to 0.1.

The advantages of using a model under the eddy viscosity hypothesis are short lived when being applied in areas of laminar flow or near walls (areas where turbulent scales are smaller). To solve this issue, a damping function, f_d is employed to properly scale Δ to match the actual effect of turbulent viscosity [49]. A Van Driest damping factor is utilized, defined as

$$f_d(y^+) = 1 - e^{-y^+/A}, \tag{3.22}$$

where A is a constant and y^+ is the non-dimensional wall distance itself, expressed by

$$y^+ = \frac{\rho_r u_\tau^d d_{wall}^d}{\mu_r}, \tag{3.23}$$

where the quantities with subscript r are the reference quantities, d_{wall}^d is the dimensional distance from the wall, and u_τ^d is the dimensional wall friction velocity. Like C_s, A is set to a specific value; in this case 25.

It is important to note that the modeled stress tensor, $\tau_{ij} - \frac{1}{3}\tau_{kk}\delta_{ij}$, is valid in the both the incompressible and compressible case. However, thanks to Erlebacher in [24], the isotropic component can be neglected when dealing with low compressible flow.

The subgrid heat diffusion flux term is taken from [23]. It follows a similar eddy viscosity model where the flux is a function of the subgrid turbulent viscosity defined by (3.21):

$$\mathcal{Q}_i^{SGS} = -\frac{1}{Pr^{SGS}}\overline{\rho}\nu^{SGS}\frac{\partial \widetilde{T}}{\partial i}, \tag{3.24}$$

where Pr^{SGS} is the subgrid Prandtl number which in this present work is set equal to the global value of 0.7.

Lastly for the turbulent diffusion flux the third order central moment $\tau(u_i, u_k, u_k)$ is neglected as done by Knight *et al* in [35] leaving

$$\mathcal{J}^{SGS} \approx 2\widetilde{u}_k\tau_{ik} + \widetilde{u}_i\tau_{kk}. \tag{3.25}$$

3.3 The Dynamic Procedure

The main drawback of the Smagorinsky model is having to rely on a constant term to describe how the subscale eddies affect the larger ones. This backscatter effect is typically not universal in time and space. In 1991, a dynamic procedure was developed by Germano *et al* in [28], based on the introduction of a second (test) filter, $\widehat{\cdot}$. This filter has its own length scale, $\widehat{\Delta}$ that is larger than the original LES filter length ($\widehat{\Delta} > \overline{\Delta}$). In addition, a second Favre filter is incorporated, indicated by the overhead symbol $\breve{\cdot}$. Analogous to the LES filtering stage, test filtered quantities can be expressed as

$$\widehat{\rho u_i} = \widehat{\rho}\breve{u}_i, \qquad \widehat{\rho e} = \widehat{\rho}\breve{e}, \qquad \widehat{\rho e_i} = \widehat{\rho}\breve{e}_i, \qquad \widehat{\rho h} = \widehat{\rho}\breve{h} = \widehat{\rho}\breve{e} + \widehat{p}. \tag{3.26}$$

The goal of the dynamic procedure is not only to develop an adjusting coefficient in time and space but also one that can be used for the test and LES filtered subgrid terms. A rule of thumb is to attempt to achieve a test filter that is twice the LES one.

The idea introduced by [28] was modified by [38] to be applicable to the Smagorinsky model. Thus, the dynamic model can be thought of an extension of the concepts developed by Smagorinsky. The LES subgrid stress tensor can then be paired with the one after applying the test filter. The expressions are as follows:

$$\tau_{ij} = \overline{\rho u_i u_j} - \overline{\rho}\widetilde{u}_i\widetilde{u}_j, \tag{3.27a}$$

$$\mathcal{T}_{ij} = \widehat{\overline{\rho u_i u_j}} - \widehat{\overline{\rho}}\breve{\widetilde{u}}_i\breve{\widetilde{u}}_j. \tag{3.27b}$$

Note the Favre filters have also been applied in (3.27). The resolved turbulent stress tensor, $\mathcal{L}_{ij}$, is defined as the difference between the test filtered and LES filtered stress tensors:

$$\mathcal{L}_{ij} = \mathcal{T}_{ij} - \widehat{\tau}_{ij} = \widehat{\overline{\rho}}\,\widetilde{\widetilde{u}_i\widetilde{u}_j} - \breve{\widehat{\overline{\rho}}}\breve{\widetilde{u}}_i\breve{\widetilde{u}}_j. \tag{3.28}$$

Since all terms on the right hand side of (3.28) are filtered LES quantities, they are known values.

The dynamic procedure begins with expressing the SGS stress tensors in (3.27) in a way analogous to Smagorinsky:

$$\tau_{ij} - \frac{1}{3}\tau_{kk}\delta_{ij} = -\overline{\rho}C_s\overline{\Delta}^2\left|\widetilde{\mathcal{S}}\right|\widetilde{\mathcal{S}}^d_{ij}, \tag{3.29a}$$

$$\mathcal{T}_{ij} - \frac{1}{3}\mathcal{T}_{kk}\delta_{ij} = -\overline{\rho}C_s\overline{\Delta}^2\left|\breve{\widetilde{\mathcal{S}}}\right|\breve{\widetilde{\mathcal{S}}}^d_{ij}. \tag{3.29b}$$

C_s, however, is no longer constant but rather defined, by means of a least squares approach, as

$$C_s = \frac{\mathcal{L}^d_{ij}\mathcal{R}_{ij}}{\mathcal{R}_{kl}\mathcal{R}_{kl}}, \tag{3.30}$$

where $\mathcal{L}^d_{ij}$ is the deviatoric part of the resolved turbulent stresses calculated with the LES variables, and

$$\mathcal{R}_{kl} = \overline{\rho}\overline{\Delta}^2\widehat{\left|\widetilde{\mathcal{S}}\right|\widetilde{\mathcal{S}}^d_{kl}} - \widehat{\overline{\rho}}\widehat{\overline{\Delta}}^2\left|\breve{\widetilde{\mathcal{S}}}\right|\breve{\widetilde{\mathcal{S}}}^d_{kl}. \tag{3.31}$$

The isotropic part, τ_{kk}, in (3.27) can be modeled in a similar fashion to the Smagorinsky subgrid stress tensor:

$$\tau_{kk} = C_I\overline{\rho}\overline{\Delta}\left|\widetilde{\mathcal{S}}\right|^2. \tag{3.32}$$

The coefficient C_I is computed dynamically according to the following expression:

$$C_I = \frac{\mathcal{L}_{kk}}{\widehat{\overline{\rho}}\widehat{\Delta}^2\left|\breve{\widetilde{\mathcal{S}}}\right|^2 - \overline{\rho}\widehat{\overline{\Delta}^2\left|\widetilde{\mathcal{S}}\right|^2}}. \tag{3.33}$$

The fact that C_s and C_I are not constant has the added bonus of removing the damping function ((3.22)) to properly model regions near walls. Moreover, the dynamic procedure allows backscatter; that is, positive work done by the subgrid stress tensor. Now, the smallest eddies can transfer energy to the larger ones within the model. This characteristic of turbulence is not negligible and is a weakness in pure eddy viscosity models that can only allow dissipation. Nevertheless, it is important to understand that the total dissipation of the flow must be positive. This restriction can be expressed with the following constraint:

$$\frac{1}{Re}\widetilde{\sigma}_{ij}\widetilde{\mathcal{S}}_{ij} - \tau_{ij}\widetilde{\mathcal{S}}_{ij} \geq 0. \tag{3.34}$$

(3.34) can be implemented by introducing a limiting coefficient:

$$\beta = \begin{cases} 1, & \tau_{ij}\widetilde{\mathcal{S}}_{ij} \geq 0 \\ \min\left(1, \frac{1}{Re}\frac{\widetilde{\sigma}_{ij}\widetilde{\mathcal{S}}_{ij}}{\tau_{kl}\widetilde{\mathcal{S}}_{kl}}\right), & \tau_{ij}\widetilde{\mathcal{S}}_{ij} > 0. \end{cases} \tag{3.35}$$

Regarding the heat and turbulent flux terms, a similar approach is taken as the SGS stress tensor. New dynamic constants are developed that are based on differences between filtered quantities and applying the least squares method. For the subgrid heat flux:

$$\mathcal{Q}^{SGS} = -\overline{\rho}\overline{\Delta}^2 \left|\widetilde{\mathcal{S}}\right| C_Q \frac{\partial \widetilde{T}}{\partial i}. \tag{3.36}$$

The coefficient C_Q can be computed locally by first calculating a temperature flux, analogous to (3.28):

$$\mathcal{L}_i^Q = \widehat{\overline{\rho}\widetilde{u}_i\widetilde{T}} - \widehat{\overline{\rho}}\breve{\widetilde{u}}_i\breve{\widetilde{T}}. \tag{3.37}$$

Applying the test filter to (2.23c) and substituting (3.36) results in

$$\widehat{\mathcal{Q}}_i^{SGS} + \mathcal{L}_i^Q = -\widehat{\overline{\rho}}\widehat{\Delta}^2\breve{\widetilde{\mathcal{S}}}C_Q\frac{\partial\breve{\widetilde{T}}}{\partial i}. \tag{3.38}$$

At this point the least squares method is applied and the expression for the heat SGS flux coefficient is given by

$$C_Q = \frac{\mathcal{L}_i^Q\mathcal{R}_i^Q}{\mathcal{R}_k^Q\mathcal{R}_k^Q}, \tag{3.39}$$

where

$$\mathcal{R}_i^Q = \widehat{\overline{\rho}\overline{\Delta}^2\widetilde{\mathcal{S}}\frac{\partial T}{\partial i}} - \widehat{\overline{\rho}}\widehat{\Delta}^2\left|\breve{\widetilde{\mathcal{S}}}\right|\frac{\partial\breve{\widetilde{T}}}{\partial i}. \tag{3.40}$$

Another departure from the Smagorinsky model is that the third order central moment in the SGS turbulent diffusion flux is no longer neglected. It is instead approximated by the following:

$$\tau(u_i, u_k, u_k) \approx \overline{\rho}\widetilde{u_i u_k u_k} - \overline{\rho}\widetilde{u_i}\widetilde{u_k u_k}. \tag{3.41}$$

Now $\tau(u_i, u_k, u_k)$ can be properly modeled:

$$\tau(u_i, u_k, u_k) = -\overline{\rho}\overline{\Delta}^2 |\mathcal{S}| C_{\mathcal{J}} \frac{\partial(\frac{1}{2}\widetilde{u_k}\widetilde{u_k})}{\partial i}. \tag{3.42}$$

Next, a kinetic energy flux is written as

$$\mathcal{L}_i^J = \widehat{\overline{\rho}\widetilde{u}_i\widetilde{u}_k\widetilde{u}_k} - \widehat{\overline{\rho}}\breve{\widetilde{u}}_k\breve{\widetilde{u}}_k\breve{\widetilde{u}}_k. \tag{3.43}$$

Following the same steps as with the SGS heat flux, the SGS turbulent flux coefficient is given by

$$C_{\mathcal{J}} = \frac{\mathcal{L}_i^{\mathcal{J}} \mathcal{R}_i^{\mathcal{J}}}{\mathcal{R}_k^{\mathcal{J}} \mathcal{R}_k^{\mathcal{J}}}, \tag{3.44}$$

where

$$\mathcal{R}_i^{\mathcal{J}} = \overline{\rho}\overline{\Delta}^2 \left|\widetilde{\mathcal{S}}\right| \widehat{\frac{\partial(\frac{1}{2}\widetilde{u}_k\widetilde{u}_k)}{\partial i}} - \widehat{\overline{\rho}}\widehat{\Delta}^2 \left|\breve{\widetilde{\mathcal{S}}}\right| \frac{\partial(\frac{1}{2}\breve{\widetilde{u}}_k\breve{\widetilde{u}}_k)}{\partial i}. \tag{3.45}$$

The dynamic procedure can lead to large fluctuations when calculating all the coefficients. Moreover, these fluctuations can occur in patches throughout the grid domain. To suppress peak values causing numerical instabilities, the dynamic procedure is averaged within each element. This maintains the flexibility without compromising the effectiveness of the method.

3.4 The Anisotropic Dynamic Procedure

The dynamic procedure previously mentioned is still unfortunately forced to be aligned with the strain rate tensor. Thus, the relation between the subgrid terms and $\widetilde{\mathcal{S}}_{ij}$ can be described only by a coefficient. This restriction is quite hindering as backscatter of energy from smaller eddies can be significant and not isotropic. Abbà *et al* in 1997 [4] first proposed to remove the alignment necessity by making the subgrid stress tensor and the strain rate tensor be related through a 4th order (symmetric) tensor:

$$\tau_{ij} = -\overline{\rho}\overline{\Delta}^2 \left|\widetilde{\mathcal{S}}\right| \mathcal{B}_{ijrs}\widetilde{S}_{rs}. \tag{3.46}$$

This new tensor, however, requires more information to construct than is readily available from the flow quantities. Some assumptions are then made to make the calculation feasible. $\mathcal{B}_{ijrs}$ is taken to be the projection of a symmetric 2nd order tensor $\mathcal{C}_{\alpha\beta}$ by an arbitrary rotation tensor a_{ij} (i.e., an orthogonal matrix with a positive determinant). This can be seen as a generalization of the diagonalization of matrices. The principal directions of $\mathcal{B}_{ijrs}$ are chosen so that when the lower rank tensor is projected, the higher order tensor is the resultant:

$$\mathcal{B}_{ijrs} = \sum_{\alpha,\beta=1}^{3} \mathcal{C}_{\alpha\beta} a_{i\alpha} a_{j\beta} a_{r\alpha} a_{s\beta}. \tag{3.47}$$

Despite the projection bases being completely arbitrary, choosing any other against the standard cartesian coordinates (δ_{ij}) did not show appreciable gains (see [2], [3], and [30]). This is partly due to the fact that $\mathcal{C}_{\alpha\beta}$ is computed through the dynamic procedure taking into the account the basis already chosen for the flow quantities.

At the initial step

$$\mathcal{C}_{\alpha\beta} = \frac{a_{i\alpha}\mathcal{L}_{ij}a_{j\beta}}{a_{r\alpha}a_{s\beta}\Big(\overline{\rho}\overline{\Delta}^2\widehat{\left|\widetilde{\mathcal{S}}\right|\widetilde{\mathcal{S}}_{rs}} - \widehat{\overline{\rho}}\widehat{\Delta}^2\left|\breve{\widetilde{\mathcal{S}}}\right|\breve{\widetilde{\mathcal{S}}}_{rs}\Big)}. \tag{3.48}$$

But due to $a_{ij} = \delta_{ij}$, the above equation simplifies to:

$$\mathcal{C}_{ij} = \frac{\mathcal{L}_{ij}}{\Big(\overline{\rho}\overline{\Delta}^2\widehat{\left|\widetilde{\mathcal{S}}\right|\widetilde{\mathcal{S}}_{rs}} - \widehat{\overline{\rho}}\widehat{\Delta}^2\left|\breve{\widetilde{\mathcal{S}}}\right|\breve{\widetilde{\mathcal{S}}}_{rs}\Big)}. \tag{3.49}$$

Now Equation (3.46) reduces to a form analogous to the eddy viscosity models in sections 3.2 and 3.3:

$$\tau_{ij} = -\overline{\rho}\overline{\Delta}^2\left|\widetilde{\mathcal{S}}\right|\mathcal{C}_{ij}\widetilde{\mathcal{S}}_{ij}. \tag{3.50}$$

Note that Equation (3.50) involves an elementwise multiplication between $\mathcal{C}_{ij}$ and $\widetilde{\mathcal{S}_{ij}}$.

Concerning the compressible flow SGS terms, a similar approach is made. The heat flux is given by

$$\mathcal{Q}_i^{SGS} = -\overline{\rho}\overline{\Delta}^2\left|\widetilde{S}\right|\mathcal{B}_{ir}^{Q}\frac{\partial\widetilde{T}}{\partial r}, \tag{3.51}$$

where

$$\mathcal{B}_{ir}^{Q} = \sum_{\alpha=1}^{3}\mathcal{C}_{\alpha}^{Q}a_{i\alpha}a_{r\alpha}, \tag{3.52}$$

and

$$\mathcal{C}_{\alpha}^{Q} = \frac{a_{i\alpha}\mathcal{L}_i^{Q}}{a_{r\alpha}\Big(\overline{\rho}\overline{\Delta}^2\widehat{\left|\widetilde{\mathcal{S}}\right|\frac{\partial\widetilde{T}}{\partial r}} - \widehat{\overline{\rho}}\widehat{\Delta}^2\left|\breve{\widetilde{\mathcal{S}}}\right|\frac{\partial\breve{\widetilde{T}}}{\partial r}\Big)}. \tag{3.53}$$

The third order central moment in $\mathcal{J}_i^{SGS}$ can be modeled with the following:

$$\tau(u_i, u_k, u_k) = -\overline{\rho}\overline{\Delta}^2\left|\widetilde{\mathcal{S}}\right|\mathcal{B}_{ir}^{\mathcal{J}}\frac{\partial(\frac{1}{2}\widetilde{u}_k\widetilde{u}_k)}{\partial r}, \tag{3.54}$$

$$\mathcal{B}_{ir}^{\mathcal{J}} = \sum_{\alpha=1}^{3} \mathcal{C}_{\alpha}^{\mathcal{J}} a_{i\alpha} a_{r\alpha}. \tag{3.55}$$

Using the dynamic procedure, the coefficient $\mathcal{C}_{\alpha}^{\mathcal{J}}$ is calculated through:

$$\mathcal{C}_{\alpha}^{\mathcal{J}} = \frac{a_{i\alpha}\mathcal{L}_{i}^{\mathcal{J}}}{\mathcal{M}_{\alpha}}, \tag{3.56}$$

where

$$\mathcal{M}_{\alpha} = a_{r\alpha}\Big(\overline{\rho}\overline{\Delta}^{2}\Big|\widetilde{\mathcal{S}}\Big|\,\frac{\widehat{\partial(\frac{1}{2}\widetilde{u_k}\widetilde{u_k})}}{\partial r} - \widehat{\overline{\rho}\overline{\Delta}^{2}}\,\Big|\breve{\widetilde{\mathcal{S}}}\Big|\,\frac{\partial\frac{1}{2}\breve{\widetilde{u_k}}\widetilde{u_k}}{\partial r}\Big). \tag{3.57}$$

Through numerous tests the Anisotropic Model was found to be more accurate and stable than the standard Dynamic Model (see [3] and [1]) but does require extra computations regarding the test filter. Nevertheless, the benefits outweigh the costs and is thus the reason for the choice of the Anisotropic model for the turbulent simulation in this thesis work.

Chapter 4

Space and Time Discretization

The Navier-Stokes equations are spatially discretized with a finite element approach, otherwise known as the Galerkin Method. In particular, a local discontinuous framework is developed analogous to the one used by Giraldo and Restelli in [32]. This chapter will discuss further the formulation of the framework and briefly how the method is implemented by the Fortran code FEMilaro [48].

4.1 The Discontinuous Galerkin Method

Before discussing the Discontinuous Galerkin (DG) method, it is beneficial to understand the general concept behind the Continuous Galerkin (CG) method first. The CG method is based on discretizing the domain on which the equations are defined on, Ω, into finite elements, K. On each of these elements basis functions are assigned that allow the representation of the solution within the element and on the element's faces. Moreover, these basis functions have the capability to span more than one element. This leads to a continuous solution all throughout the domain. A thorough explanation of the CG method and its application can be found in [68].

The DG method, on the other hand, utilizes basis functions that support only one element. Due to the independence of elements, basis functions can be individually assigned making the DG method an ideal environment for mesh and degree adaptivity.

Another fundamental characteristic of the DG method is its ability to conserve mass locally through the use of numerical fluxes. The flux associated with each element face requires information regarding only its imme-

diate neighbors regardless of the order of accuracy. It can be seen how the DG method is desirable as it allows for high parallelization on computers. More details about the derivation and theory behind the DG method are explained in [18]

One of the first implementations of the DG method was done by Reed and Hill in [45] for hyperbolic transport equations. Combining the DG approach with a stable time discretization and guidelines for computing numerical fluxes, both occurring locally, leads to the Local Discontinuous Galerkin (LDG) method employed in this work. A more detailed description on how the LDG approach was developed for various partial differential equations can be found in [19], [11], and [7]. Regarding the compressible Navier-Stokes equations, a framework was developed proposed in [9]. Here, the solution and the gradient of the solution are formed from discontinuous bases. Before discussing how the LDG method is formulated, Equation (2.23) is rewritten in the following way:

$$\frac{\partial \boldsymbol{U}}{\partial t} + \nabla \cdot \boldsymbol{F}^c(\boldsymbol{U}) = \nabla \cdot \boldsymbol{F}^v(\boldsymbol{U}, \nabla \boldsymbol{U}) - \nabla \cdot \boldsymbol{F}^{SGS}(\boldsymbol{U}, \nabla \boldsymbol{U}) + \boldsymbol{S}, \tag{4.1}$$

where $\boldsymbol{U}$ is the vector containing the conserved quantities (density, momentum, energy); $\boldsymbol{F}$ are the flux terms, c denoting convective flux and d diffusive flux; $\boldsymbol{F}^{SGS}$ is the flux due to the effects of subgrid terms; and $\boldsymbol{S}$ are any source terms present in the domain under consideration. Expressions for these vectors are found below:

$$\boldsymbol{U} = \begin{bmatrix} \overline{\rho} \\ \overline{\rho}\widetilde{\boldsymbol{u}} \\ \overline{\rho}\widetilde{e} \end{bmatrix}, \tag{4.2}$$

$$\boldsymbol{F}^c = \begin{bmatrix} \overline{\rho}\widetilde{\boldsymbol{u}} \\ \overline{\rho}\widetilde{\boldsymbol{u}} \times \widetilde{\boldsymbol{u}} + \frac{1}{\gamma Ma^2}\overline{p}\mathcal{I} \\ \widetilde{\overline{\rho}h}\widetilde{\boldsymbol{u}} \end{bmatrix}, \tag{4.3}$$

$$\boldsymbol{F}^d = \begin{bmatrix} 0 \\ \frac{1}{Re}\widetilde{\sigma} \\ \frac{\gamma Ma^2}{Re}\widetilde{\boldsymbol{u}}^T\widetilde{\sigma} - \frac{1}{\kappa RePr}\widetilde{\boldsymbol{q}} \end{bmatrix}, \tag{4.4}$$

$$\boldsymbol{F}^{SGS} = \begin{bmatrix} 0 \\ \tau \\ \frac{1}{\kappa}\boldsymbol{\mathcal{Q}}^{SGS} + \frac{\gamma Ma^2}{2}(\boldsymbol{\mathcal{J}}^{SGS} - \tau_{kk}\widetilde{\boldsymbol{u}}) \end{bmatrix}, \tag{4.5}$$

The LDG method, described by Cockburn in [19], states that the second order partial differential equation being studied is reformulated as a first order system by introducing a new gradient term. Equation (4.1) then becomes

$$\begin{aligned}\frac{\partial \boldsymbol{U}}{\partial t} + \nabla \cdot \boldsymbol{F}^c(\boldsymbol{U}) =& \nabla \cdot \boldsymbol{F}^v(\boldsymbol{U}, \boldsymbol{\mathcal{G}}) - \nabla \cdot \boldsymbol{F}^{SGS}(\boldsymbol{U}, \boldsymbol{\mathcal{G}}) + \boldsymbol{S}, \\ \boldsymbol{\mathcal{G}} - \nabla \boldsymbol{\varphi} &= 0, \end{aligned} \tag{4.6}$$

where $\boldsymbol{\varphi} = \begin{bmatrix} \widetilde{\boldsymbol{u}}, & \widetilde{T} \end{bmatrix}^T$, quantities that appear in the diffusive and SGS fluxes under the gradient operator.

The next step is to define the suitable subspace for the finite elements, $\mathcal{V}_h$. With the domain represented by Ω and the discretization by $\mathcal{T}_h$,

$$\mathcal{V}_h = \{v_h \in L^2(\Omega) : v_h|_K \in \mathbb{P}^q(K), \forall K \in \mathcal{T}_h\}, \tag{4.7}$$

where $\mathbb{P}^q$ is the space of polynomials that is set on the element K with degree equal to q.

With the finite element space defined, the weak discrete form of the Navier-Stokes equations can be obtained. The test functions are v_h and $\boldsymbol{r}_h$ corresponding to the conserved quantities and gradient terms. The outward unit normal vector is represented by $\boldsymbol{n}_{\partial K}$ where ∂K represents the boundary of the element. Integrating over all the element boundaries within our discretized domain the following is obtained:

$\forall K \in \mathcal{T}_h, \forall v_h \in \mathcal{V}_h, \forall \boldsymbol{r}_h \in \mathcal{V}_h,$

$$\begin{aligned} \frac{d}{dt}\int_K \boldsymbol{U}_h v_h d\boldsymbol{x} - \int_K \boldsymbol{F}(\boldsymbol{U}_h \boldsymbol{\mathcal{G}}_h) \cdot \nabla v_h d\boldsymbol{x} \\ + \int_{\partial K} \widehat{\boldsymbol{F}}\left(\boldsymbol{U}_h, \mathcal{G}\right) \cdot \boldsymbol{n}_{\partial K} v_h d\sigma = \int_K \boldsymbol{S} v_h d\boldsymbol{x}, \end{aligned} \tag{4.8a}$$

$$\begin{aligned} \int_K \boldsymbol{\mathcal{G}} \cdot \boldsymbol{r} d\boldsymbol{x} + \int_K \boldsymbol{\varphi} \nabla \cdot \boldsymbol{r}_h d\boldsymbol{x} \\ - \int_{\partial K} \widehat{\boldsymbol{\varphi}}\, \boldsymbol{n} \cdot \boldsymbol{r}_h d\sigma = 0, \end{aligned} \tag{4.8b}$$

where the discrete conserved quantities, $\boldsymbol{U} = \begin{bmatrix} \rho_h, & \rho \boldsymbol{u}_h, & \rho e \end{bmatrix}^T$, $\boldsymbol{\varphi} = \begin{bmatrix} \boldsymbol{u}_h, & T_h \end{bmatrix}^T$, and $\boldsymbol{F} = \boldsymbol{F}^c - \boldsymbol{F}^d + \boldsymbol{F}^{SGS}$. The numerical flux terms are given by $\widehat{\boldsymbol{F}}$ and $\widehat{\boldsymbol{\varphi}}$. Recall it is the numerical flux that couples neighboring elements together thereby conserving mass. A Rusanov flux scheme is employed for $\widehat{\boldsymbol{F}^c}$ while a centered scheme is used for diffusive fluxes, $\widehat{\boldsymbol{F}^d}$, $\widehat{\boldsymbol{F}^{SGS}}$ and the gradient term flux, $\widehat{\boldsymbol{\varphi}}$.

The Rusanov flux scheme can be expressed in a similar manner to [32] by the following:

$$\widehat{\boldsymbol{F}^c} = \frac{1}{2}[F_L^c + F_R^c + |\lambda|(\boldsymbol{U}_L \boldsymbol{n}_{\partial K,L} + \boldsymbol{U}_R \boldsymbol{n}_{\partial K,R})], \tag{4.9}$$

where $\lambda = \max(U + \sqrt{a^L}\ ,\ U + \sqrt{a^R})$ with $U^{L/R} = \boldsymbol{u}^{L/R} \cdot \boldsymbol{n}$ being the normal component of velocity on the edge of the boundary ∂K, and $a^{L/R}$ the speed of sound.

Despite being rather simple, other more complex models used in [32] and [31] did not show appreciable gains in stability or accuracy.

The centered fluxes are given by averages:

$$\widehat{\boldsymbol{F}^v} = \frac{1}{2}(\boldsymbol{F}_L^v + \boldsymbol{F}_R^v), \tag{4.10}$$

$$\widehat{\boldsymbol{F}^{SGS}} = \frac{1}{2}(\boldsymbol{F}_L^{SGS} + \boldsymbol{F}_R^{SGS}), \tag{4.11}$$

$$\widehat{\boldsymbol{\varphi}} = \frac{1}{2}(\boldsymbol{\varphi}_L + \boldsymbol{\varphi}_R). \tag{4.12}$$

The basis for the finite element space will be generated by an extension of the orthonormal Legendre polynomials. It is with this set of polynomials that the approximate solution will be reconstructed. A generic quantity a can be expressed as:

$$a_h|_K = \sum_{i=0}^{n_\phi(K)} a^i \phi_i^K, \tag{4.13}$$

where ϕ are the basis functions prescribed on element K, a^i are the modal coefficients, and $n_\phi(K) + 1$ is the number of polynomials required to span the space $\mathbb{P}^{q_K}$. $n_\phi(K)$ can be determined for $\mathbb{R}^3$ by the following formula

$$n_\phi(K) = \frac{1}{6}(q_K + 1)(q_K + 2)(q_K + 3) - 1 \tag{4.14}$$

The accuracy of the approximate solution can be increased by increasing the degree of the polynomial space and by extension the degree of polynomials within the basis.

Equation (4.13) can be rewritten, when a hierarchical basis is adopted, as

$$a_h|_K = \sum_{p=0}^{q_K} \sum_{l \in d_p} a^{(l)} \phi_l^K, \tag{4.15}$$

where $d_0 = \{0\}$ and

$$d_p = \{l \in 1 \dots n_\phi(K) \mid \phi_l \in \mathbb{P}^p(K) \backslash \mathbb{P}^{p-1}(K)\} \tag{4.16}$$

is the set of indices for the basis functions of degree p. This formulation means that if a more or less accurate approximation is desired, then p is summed over a larger or smaller limit q_K.

Regarding LES filtering, a projection operator Π is constructed as in [62], represented as $\Pi : L^2(\Omega) \to \mathcal{V}$ and defined by

$$\int_\Omega \Pi uvd\boldsymbol{X} = \int_\Omega uvd\boldsymbol{X}, \forall u, v \in \mathcal{V}. \tag{4.17}$$

If the LES filter, $\bar{\cdot}$, is considered to be a projection over the finite element subspace $\mathcal{V}_h$ then the approximate solution coefficients $\overline{a}$ can be expressed as

$$\overline{a} = \Pi_{\mathcal{V}_h} a \tag{4.18}$$

Note that (4.18) is written simply for formality. When (3.19) are spatially discretized the LES projection has been performed and the approximate solution is the filtered one.

The last point to be discussed is the LES filter length itself. It has been discussed in great detail in Chapter 3 exhibiting its importance in all the SGS models. $\overline{\Delta}$ or for that matter $\widehat{\Delta}$ cannot be known *a priori* to ensure a certain percentage of eddy scales are resolved. In this work, the filter length is taken to be constant and to account for the anisotropy of the grid, whose expression is provided by [52]:

$$\Delta(K) = \sqrt[3]{\frac{Volume(K)}{n_\phi(K)+1}}. \tag{4.19}$$

4.2 Polynomial Adaptivity

When solving partial differential equations numerically, simple grid refinement tends towards a DNS solution [49], [20]. Two approaches are therefore used to obtain a more time saving accurate solution. The first is h-adaptivity. Here, the computational grid is altered at certain time intervals by breaking or combining local subdomains; swapping or collapsing edges; or redistributing the location of nodes. Examples are given in [46] and [47]. Although efficient and effective, h-adaptivity does have certain drawbacks. The solution needs to be interpolated every time a new mesh is computed. Thus, complex data structures need to be maintained to keep track of the number of nodes, edge connectivity, areas, and volumes.

Methods based on defining the variables with a functional basis such as the CG and DG methods, offer another adaptivity approach: p-adaptivity. In this case, the degree of polynomials that form the basis for the solution on the finite element is altered. The application of this feature for finite elements was first done by Zienkiewicz *et al* in [67] and in [69]. p-adaptivity can be implemented by assigning the degree for each element based on some indicator being within certain thresholds. In a DG framework, p-adaptivity is even more desirable since elements do not require to have the same polynomial degree basis. This allows for local adjustment of the polynomial order only where it is necessary. The limitation of p-adaptivity is the practicality of having excessive polynomial degrees within an element. A thorough comparison between h and p-adaptivity was done by Chapelier in [13] for DG simulations.

The process of p-adaptivity can be further simplified if a modal DG approach is taken. Since the solution is the sum of constant coefficients multiplied by a set of orthogonal polynomials, increasing the order only means adding extra coefficients initialized to zero. For reducing the polynomial degree, it is explained by Remacle in [46] that the higher order coefficients can be discarded to obtain the definition of the solution interpolated on the new basis.

The remaining topic of discussion is the indicator itself. For this work, an indicator based on the relative weight (RW) of modal coefficients is employed similar to the ones in [61] and [60]. The indicator is defined as

$$Ind_{RWM}(K) = \sqrt{\frac{e^s(K)}{e^*(K)}}, \tag{4.20}$$

where $e^{*/s}$ is a pseudo-energy based on the momentum of all and the smallest scales, respectively. Their individual expressions are given by

$$e^*(K) = \sum_{i=1}^{3} \int_K (\rho u_i)'(\rho u_i)' dv, \tag{4.21}$$

$$e^s(K) = \sum_{i=1}^{3} \int_K (\rho u_i)^s (\rho u_i)^s dv, \tag{4.22}$$

where the $'$ symbol represents the value of momentum after the mean value over the element has been subtracted and the superscript s indicates the smallest scale contribution. Equations (4.21) and (4.22) are nothing more than the sum of the modal coefficients associated to the basis functions of degrees larger than zero. Denoting $m_i^{(l)}$ the modal coefficients of the

i^{th} component of momentum and using the representation in (4.15), Equations (4.21) and (4.22) can be expressed as

$$e^*(K) = \sum_{i=1}^{3} \sum_{l=1}^{n_\phi(K)} (m_i^{(l)})^2, \tag{4.23}$$

$$e^s(K) = \sum_{i=1}^{3} \sum_{l \in d_{q_K}} (m_i^{(l)})^2, \tag{4.24}$$

where the smallest scales have been identified with the modal contributions with the highest polynomial degree over the element.

The relative weight indicator is based on the momentum rather than the velocity since the modal coefficients are readily available and no additional computations are required. The momentum, fortunately, carries similar information as the velocity. The mean value within the element is removed in the total pseudo-energy to avoid the under-weighting of areas with strong mean flow. If not removed, then a mean flow field with large variations could affect the indicator. This was also done to conserve Galilean invariance akin to Flad *et al* in [26].

For this thesis work, p-adaptivity was utilized only for the laminar simulations. Therefore, the indicator (4.20) resembles the one used by Eskilsson in [25]. The sum of modal contributions can be seen as the L^2 norm of the momentum variable, and the contribution of the highest degree is that of the difference between itself and the degree -1 approximation. The error of the solution is then controlled by imposing suitable thresholds.

p-adaptivity can be performed intermittently or during run time. In the former case, a simulation is run for a small time length to calculate a sample of indicator values. This collection is averaged in time then compared to the specified thresholds, adjusting the polynomial degree where necessary. The simulation is resumed according to the new degree distribution. It is common to rebalance the number of degrees of freedom with parallel runs among the various processors. This ensures no one processor is overloaded with computations increasing efficiency. These *static* adaptive simulations are best suited for steady flow scenarios. If the flow is heavily transient or turbulent, *dynamic* adaptivity must be used.

Dynamic adaptivity works similarly to static adaptivity. The principle of calculating many indicators then averaging the values is maintained. But now the numerical implementation automatically adjusts the polynomial degrees. The indicator is sampled higher than the time step to remove any transient effects. The same reasoning is made for the actual adaptation

intervals. The process of dynamic adaptation is as follows: given an indicator calculation time step, Δt_i, and solution adaptation time step, Δt_a; a minimum and maximum polynomial degree: p_{min} and p_{max}; an array of thresholds, ϵ, whose length is one less than the number of polynomials in $[p_{min}, p_{max}]$:

1. If the current time is a multiple of Δt_i then calculate and store the indicator value.

2. If the current time is a multiple of Δt_a average the indicator values.

3. Assign the degree corresponding to the range of thresholds in which the indicator falls. If the indicator is above the maximum threshold assign the element p_{max}. If the indicates is below the minimum threshold assign the element p_{min}.

Calculation of the thresholds is not trivial and must be delt with care as minute changes can have profound effects in the distribution of the degrees of freedom. A procedure for determining threshold values is explained by Tugnoli *et al* in [59]. The process begins with a static assessment of the flow, calculating the average indicator value over a small amount of time. Then the indicator is compared to a series of thresholds and seeing how many elements have indicators above said threshold. Ideally, the thresholds should be chosen such that the total amount of degrees of freedom is around the same as a lower polynomial order.

The strategy behind the choosing the time interval for calculating the indicator and adapting the solution is highly case sensitive. A sample of the thought process can be found in the work of Abbà, Recanti, Tugnoli, and Bonaventura in [5]. The procedure for determining Δt_i and Δt_a for this work will be explained in Chapter 5.

At the current moment, FEMilaro does not have a dynamic load balancing procedure for parallel simulations. This means it is possible during runtime, to have one or a few processors with a majority of the degrees of freedom and the remaining processors waiting in idle. Nevertheless, the advantages of dynamically adapting the solution proved to be significant in the tests conducted and the results are presented in Chapter 5.

4.3 Time Integration

The spatial discretization is advanced in time through a 5 stage, 4th order, and explicit Strong Stability Preserving Runge-Kutta (SSPRK) method

from Spiteri and Ruuth in [55]. The idea behind using this method comes from the necessity to reduce spurious oscillations due to discontinuities such as shock waves. Traditional Total Variational Diminishing (TVD) schemes aim to reduce the presence of these oscillations by ensuring the following:

$$TVD(U^{n+1}) \leq TVD(U^n). \tag{4.25}$$

(4.25) serves as a norm and condition for which the time discretization scheme must uphold. If (4.25) is satisfied, then the numerical time scheme is said to be strong stability preserving. Despite the test cases presented in this work being in the laminar regime FEMilaro is a compressible flow solver. Therefore, it was essential to use a TVD time scheme as to reduce any discontinuities arising from compressibility effects.

In addition, multistep high order Runge-Kutta schemes offer good efficiency. The solution proposed in [55] proved that the gains in increasing the time step was greater than the penalty taken from the additional calculations. More about the time step used in the simulations will be discussed in the next chapter.

4.4 Numerical Implementation

The numerical methods discussed in this chapter are implemented by the finite element toolkit, FEMilaro [48]. This code utilizes the latest Fortran features namely, object oriented programming. The code is maintained by members in the Aerospace and Technology and Mathematics department at the Politecnico di Milano and the Max-Planck-Institut für Plasmaphysik. The parallelization capabilities are performed by an OpenMPI framework.

The mesh was generated with the open source software Gmsh [29]. Details on the actual geometry will be discussed in Chapter 5. Grid partitioning was performed with the METIS library [34]. This library cleverly divides the mesh in order to minimize the number of points that have to communicate between processors. This greatly improves the efficiency and scalability of the MPI framework.

Chapter 5

Flow Past A Rotating Cylinder

5.1 2D Laminar Simulations with Non-Constant Rotation

This work sought to replicate the results of Choi *et al* in [16] by implementing the p-adaptive model proposed in [9] using the FEMilaro library. The cylinder in Figure 1.1 will undergo harmonic rotary oscillation with a dimensional rotational speed, ω_0. The parameter α, defined in (1.4), is then rewritten in the following way:

$$\alpha = \frac{\omega_0 D}{2U_\infty}. \tag{5.1}$$

In [16], a forcing Strouhal number to which the cylinder will be subjected to is given by

$$St_f = \frac{f_f D}{U_\infty}, \tag{5.2}$$

where f_f is the frequency of the forced oscillation. α pulsates according to the following relation:

$$\alpha = \Omega \sin(2\pi St_f t), \tag{5.3}$$

where Ω is the maximum amplitude of the non-dimensional rotation rate (Equation (5.1)) and t represents the non-dimensional time. For this section, the Mach number is kept at 0.15 to ensure compressibility effects are negligible.

A rectangular domain was used in all the computations. The domain is sketched in Figure 5.1 and the dimensions for the different meshes are given in Table 5.1. Each length is nondimensionalized by the cylinder diameter, which is set to 1.

$Mesh$	L_f	L_r	L_s
1	10	20	10
2	20	40	20

Table 5.1: Dimensions for Computational Domain

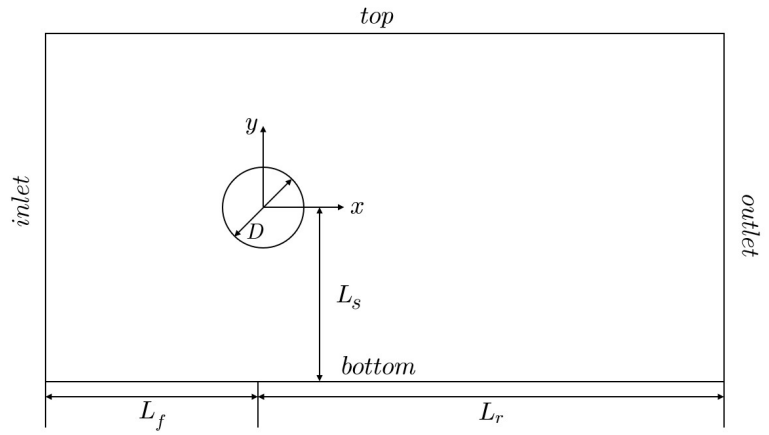

Figure 5.1: Computational Domain for 2D Laminar Simulations

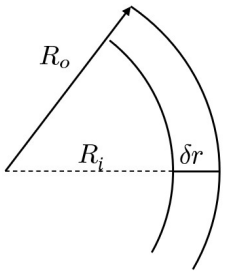

Figure 5.2: Cylinder Boundary

Table 1 in [16] reports the radial and angular distance between nodes on the boundary surface of the cylinder. Even though unstructured meshes with unequal elements are used, an equivalent spacing can be calculated considering the order of the polynomial basis. An annular region was constructed around the cylinder to ensure proper capture of the boundary layer (see Figure 5.2). As in [16], the following parameters are defined:

$$\Delta r_b = \frac{\delta r}{(N_{ar} - 1)k}, \tag{5.4}$$

$$\Delta \theta_b = \frac{360^\circ}{N_c k}, \tag{5.5}$$

where δr is the radial thickness of the annular region, N_{ar} is the number of nodes along δr, N_c is the number of nodes on the cylinder surface, and k is the polynomial degree.

Dirichlet boundary conditions were imposed on all the boundaries. The inlet was set to the normalized freestream velocity, itself equal to 1, while the velocities at the top, bottom, and outlet were set to zero. On the surface of the cylinder, a time dependent dimensional velocity was imposed, given by

$$u_\theta^d = \frac{\omega_0 D}{2} \sin(2\pi St_f t). \tag{5.6}$$

Since the velocity is normalized with respect to the freestream value i.e., $V_r = U_\infty$ in Equation 2.21a, the actual boundary condition applied is

$$u_\theta = \Omega \sin(2\pi St_f t). \tag{5.7}$$

The FEMilaro toolkit uses a Cartesian frame of reference and as a consequence, u_θ must be decomposed into its x and y components. Assuming the rotation is counterclockwise,

$$\begin{aligned} u_x &= -u_\theta \sin(\theta), \\ u_y &= u_\theta \cos(\theta), \end{aligned} \tag{5.8}$$

where θ is the counterclockwise angular position of each node on the cylinder's surface.

To save time and speed up convergence of the various statistics, only the degree 2 simulation was carried out for an extended period of time. The higher order simulations were instead initialized from the degree 2 solution. For all the 2D experiments, the maximum amplitude for the rotary oscillation, Ω, was set to 2.

5.1.1 $Re = 100$, $St_f = 0.4$

Two meshes composed of triangles were used: mesh 1 with 960 elements and mesh 2 with 1184 elements. Values for the mesh metrics; mean drag and

fluctuating lift force coefficients; and vortex shedding frequency are reported in Table 5.2 for the different polynomial degrees used in the simulations. The simulation was advanced in time with a non-dimensional time step of 10^{-3} for degrees 2 and 3; and 8×10^{-4} for degree 4.

$Mesh$	k	$DOFs$	Δr_b	$\Delta\theta_b$	C_l'	$\overline{C_d}$	St_{vs}
	2	5760	0.0250	2.813°	0.328	1.336	0.4
1	3	9600	0.0167	1.875°	0.322	1.327	0.4
	4	14400	0.0125	1.406°	0.322	1.327	0.4
	2	7160	0.0500	5.000°	0.328	1.271	0.4
2	3	11840	0.0333	3.333°	0.316	1.260	0.4
	4	17760	0.0250	2.500°	0.317	1.261	0.4

Table 5.2: Values for $Re = 100$ and $St_f = 0.4$ for various polynomial degrees

Increasing the polynomial order beyond 3 showed little improvement on the values of the statistics signaling that degree independence has been reached for both meshes. This implies the grid resolution is sufficient to reach a steady value.

The errors comparing the obtained values with degree $k = 4$ to those in [16] are listed in Table 5.3. Both the fluctuating lift and drag are deemed sufficiently accurate, especially when considering the amount of degrees of freedom used in the present work compared to that of [16]. Both coefficients exhibit a quite interesting characteristic as mesh 2 with larger dimensions produced values closer to those reported in [16] (1.236 for $\overline{C}_d$ and 0.301 for C_l'). Another simulation with smaller dimensions and a higher resolution compared to mesh 1 and 2 was performed to identify the cause of this trend. The resulting drag and lift coefficient were larger than mesh 1, highlighting the fact that the boundaries influenced the flow development and that a larger computational domain was necessary.

$Mesh$	$C_{l'_{err}}$	$\overline{C_{derr}}$	$St_{f_{err}}$
1	8.9%	18.9%	0.0%
2	5.2%	4.3%	0.0%

Table 5.3: Error values for constant $k = 4$ simulations: $Re = 100$, $St_f = 0.4$

Figure 5.3 plots the time averaged lift coefficient for the last 10 time units of the degree 2 simulation for mesh 1. Notice that the mean value is not

tending towards zero as theory predicts [42]. This discrepancy is attributed to the small number of elements in the vicinity of the cylinder. Increasing the polynomial order resulted in a mean value closer to zero.

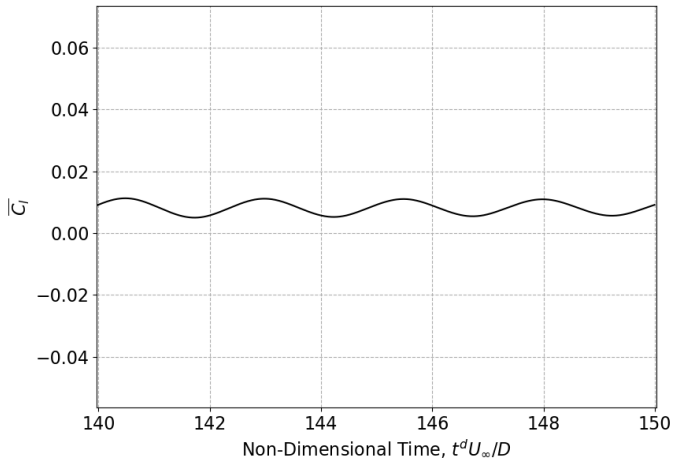

Figure 5.3: Time history of mean lift coefficient: $Re = 100$ and $St_f = 0.4$ for degree = 2

Figure 5.4 plots the coefficient of drag versus the coefficient of lift for a section of simulation time. The smooth pathlines indicate that statistical convergence was attained. In addition, the plots highlight the effect of the non-zero mean lift, causing the degree 2 orbital graph to be slightly nonsymmetric.

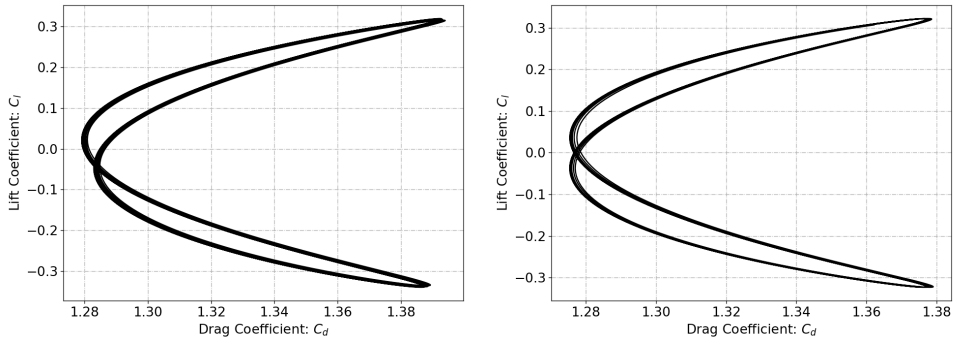

(a) $k = 2$ (b) $k = 4$

Figure 5.4: C_d vs. C_l Orbits for mesh 1, $Re = 100$, and $St_f = 0.4$

From this point on, the remaining results are from the mesh 2 simulation in which the force statistics were the closest to those of [16].

The time history of the lift and drag are shown in Figure 5.5. It can be

observed that both the force coefficients have reached a quasi-steady-state oscillating around a constant mean.

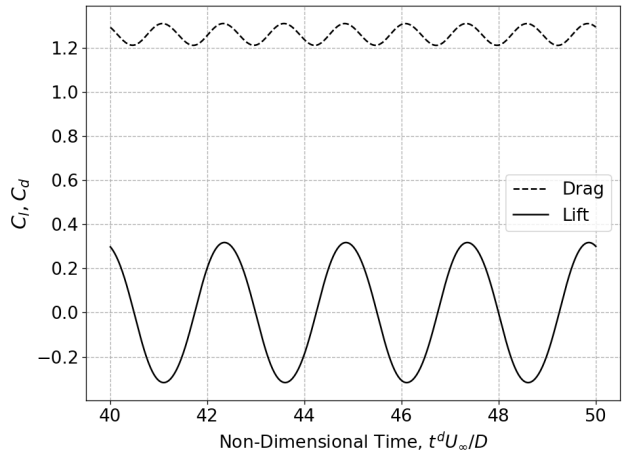

Figure 5.5: Time history of lift and drag coefficients for $k = 4$, $Re = 100$, and $St_f = 0.4$

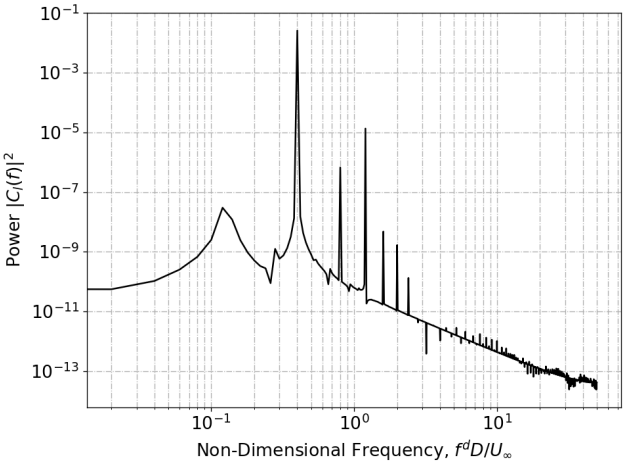

Figure 5.6: Power Spectra for Force Coefficients: $Re = 100$ and $St_f = 0.4$

The force coefficients were calculated with a time step of 0.01 to ensure that a wide range of frequencies were captured. Figure 5.6 displays the lift power spectrum for the $k = 2$ simulation. The peak amplitude is quite visible, along with smaller peaks denoting the integer multiples of the shedding frequency. The vortex shedding Strouhal number matches the forced one, signaling that the phenomenon known as lock-on or synchronization

occurred.

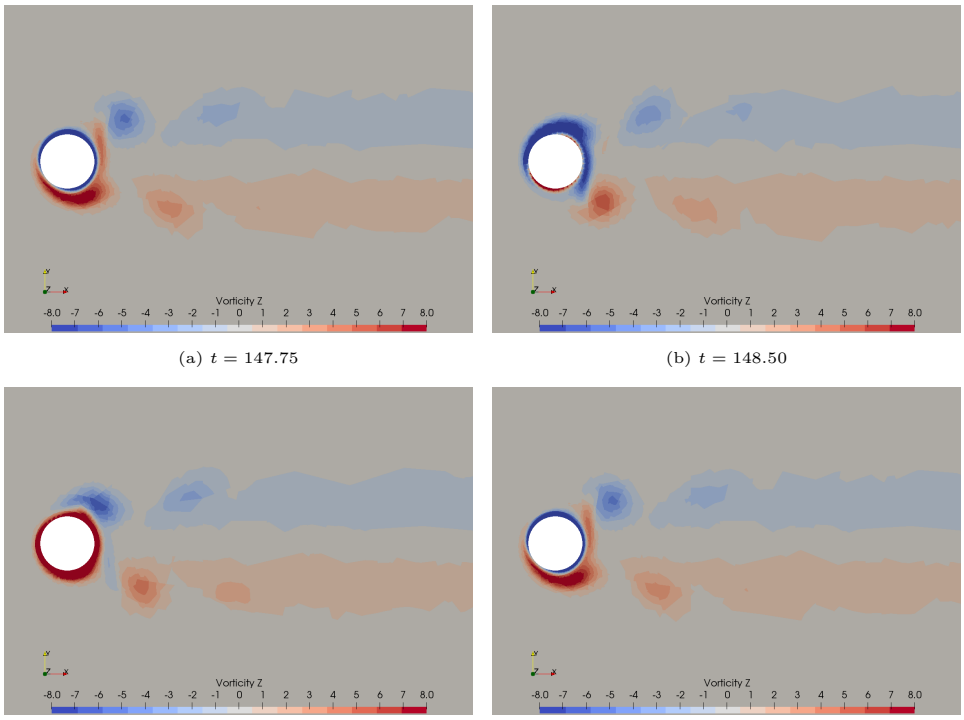

(a) $t = 147.75$ (b) $t = 148.50$

(c) $t = 149.25$ (d) $t = 150.00$

Figure 5.7: Vorticity contours for degree 4: $Re = 100$ and $St_f = 0.4$

Figure 5.7 displays the vorticity contours at various time intervals. The plots have been scaled to allow a better visualization of the shedding vortices. The plots match well with [16], depicting two clear regions of positive and negative vorticity, below and above the cylinder, respectively. The top and bottom vortices do not interact as they are controlled by the cylinder's rotary oscillation. Only after a sufficiently long distance behind the cylinder do the vortices coalesce into a more traditional Von Kármán vortex street (Figure 5.9).

Figure 5.8 instead illustrates the sensitivity to the variation of the polynomial degree. The higher order polynomial degrees produced a noticeable improvement in the visual representation of the flow. More importantly, Figure 5.8 highlights the potential for p-adaptivity. If the polynomial degree can change only within the wake regions, then quality statistics can be obtained while at the same time reducing the computational cost with respect to the constant degree simulation.

To emphasize the prospect of significant computational time savings using degree adaptivity, another simulation was run with constant polynomial

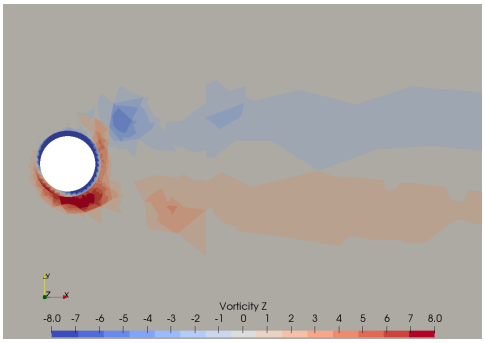

(a) $k = 2$

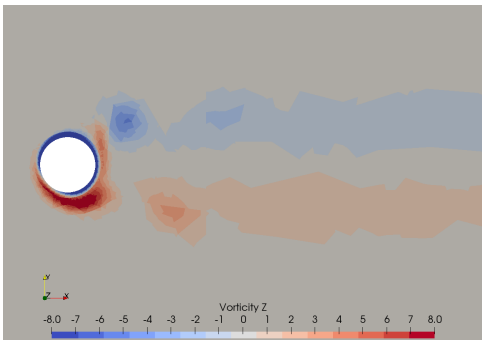

(b) $k = 3$

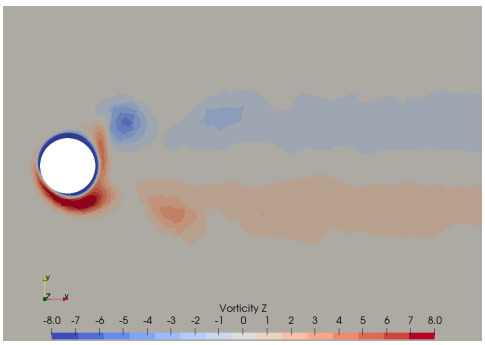

(c) $k = 4$

Figure 5.8: Vorticity Comparison for Various Constant Degrees

order 5. Only mesh 2 was considered for the adaptive simulations since the corresponding lift and drag coefficients were the closest to those reported in [16]. The RW Modal indicator defined in (4.20) was then calculated based on the output of the last time step for all degrees. It was stated previously that for the Ω, Re, and St_f under consideration, vortex shedding frequency synchronization was obtained. It was determined that a Δt_a of 0.05 would be sufficient to simulate properly the flow, because the trailing vortices shed at a rate of 0.4 (corresponding to a period of 2.5 time units). To remove the time dependency from the indicator, a Δt_i of 2×10^{-3} was chosen to supply

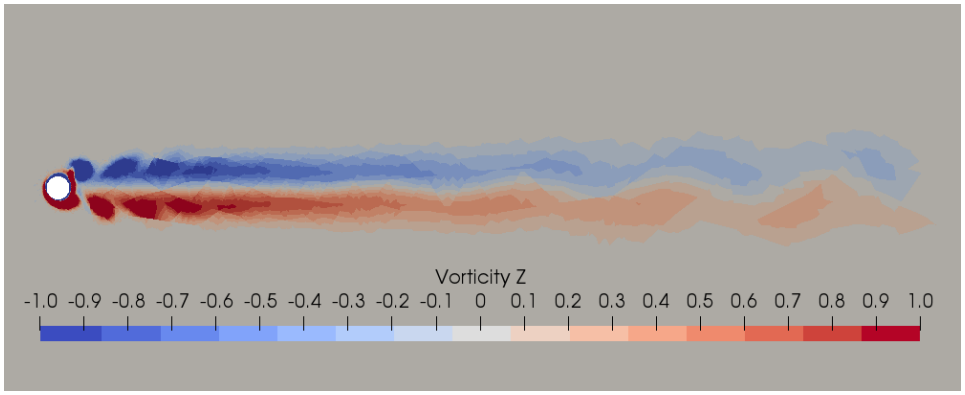

Figure 5.9: Cylinder wake: $Re = 100$ and $St_f = 0.4$

an ample amount of values for averaging. Figure 5.10 shows the values of the indicator for one adaptation step and degree 4. The global time step was set to 5×10^{-4}.

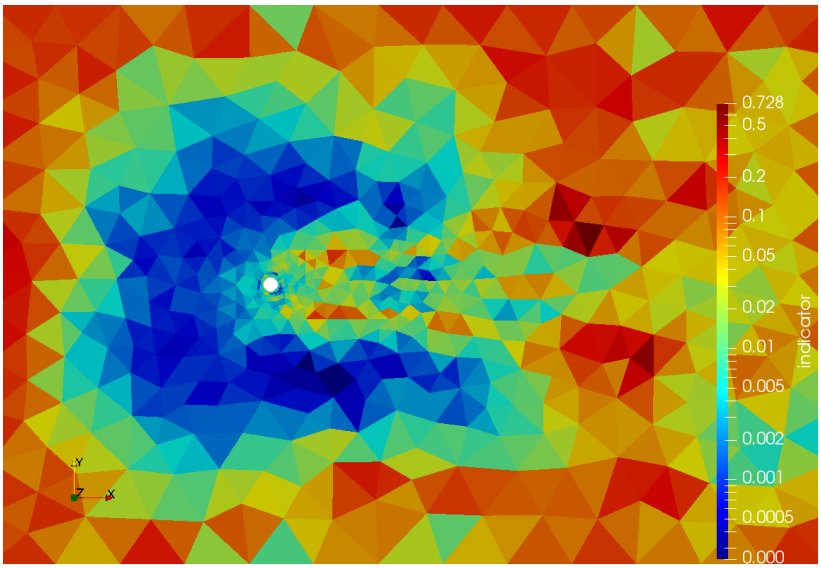

Figure 5.10: Logarithmic contour plot of the RW Modal Indicator for $k = 4$, $Re = 100$, and $St_f = 0.4$

The contour plot of the indicator also serves as a way to visualize where adaptivity is required. Since the interaction between the cylinder and the flow create a wake, higher values of the indicator are to be expected in this region, similar to that of [59]. Figure 5.10 does not match exactly due to the present flow being well in the laminar regime. The indicator nonetheless denotes elements behind the cylinder in need of degree refinement and

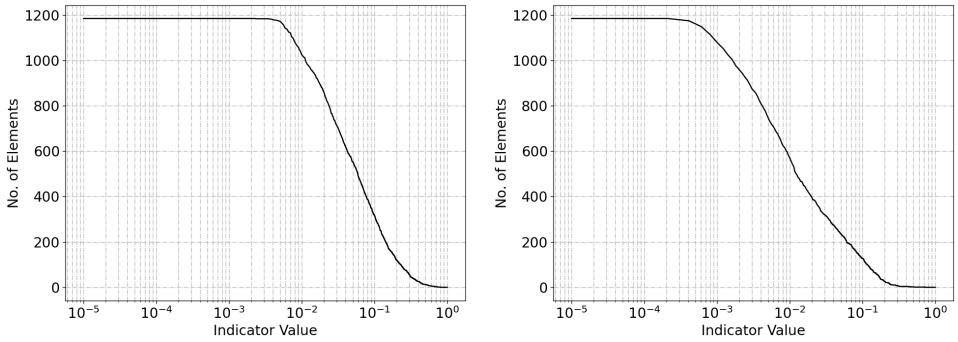

(a) $k = 3$ (b) $k = 4$

Figure 5.11: No. of elements above a certain indicator: $Re = 100$ and $St_f = 0.4$

elements ahead of the cylinder for degree coarsening.

Figure 5.11 displays the number of elements above a certain indicator value. This plot helps in the choice of the thresholds to be employed in the adaptive simulations. In this work, the polynomial degree spans from 2 to 5. Therefore, three thresholds were chosen: $\epsilon_1 = 0.01$, $\epsilon_2 = 0.08$, and $\epsilon_3 = 0.15$. These values resulted in a total amount of degrees of freedom of around 12400, roughly equivalent to the $k = 3$ case.

The adaptive simulation was initialized with the output of a $k = 2$ simulation run up to 50 time units.

Table 5.4 reports the values of force coefficients along with the Strouhal number for the adaptive simulation compared with those of the constant $k = 5$ degree simulation. Notice how the resulting values agree well with the constant degree simulations while reducing the average time to compute one time step, $\bar{t}_{step}$, by 46.6%.

	$DOFs$	C_l'	$\overline{C_d}$	St_{vs}	$\bar{t}_{step}$
$k = 5$	24864	0.317	1.260	0.4	$0.408s$
$k = 2$ To 5	12400	0.317	1.262	0.4	$0.218s$

Table 5.4: Values for the adaptive simulation $Re = 100$ and $St_f = 0.4$ for $k = 2$ to 5

Figure 5.12 shows the polynomial distribution at one of the initial time steps. The adaptation results in higher order polynomials in the same two distinct regions where the trailing vortices were observed in Figure 5.7. The indicator values for the adapted elements remains in the corresponding threshold range maintaining the high level of accuracy. Figure 5.13 zooms in on the cylinder to visualize the adaptation at the first few time

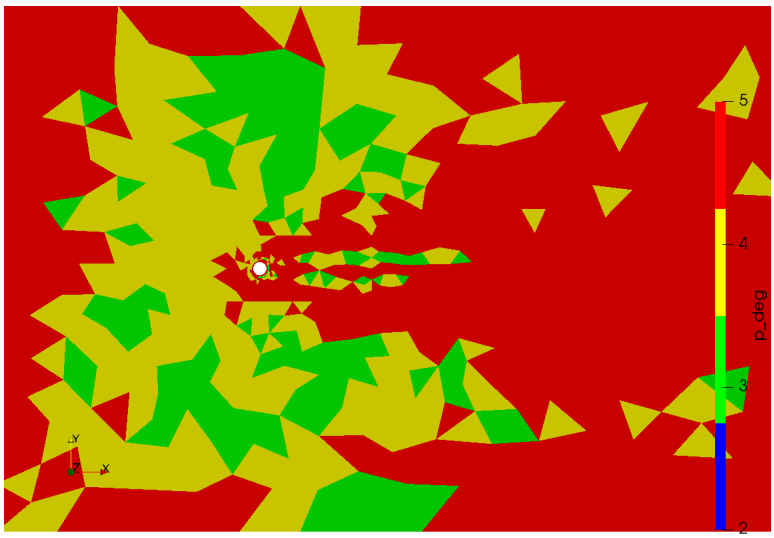

Figure 5.12: Adaptation step $t = 0.1$

steps. Because the adaptive simulation is initialized from the $k = 2$ solution, the adaptive process overcompensates and assigns mostly degree 5 elements throughout the domain. Only after a few adaptation steps does the solver adjust and increase the polynomial order in the required locations.

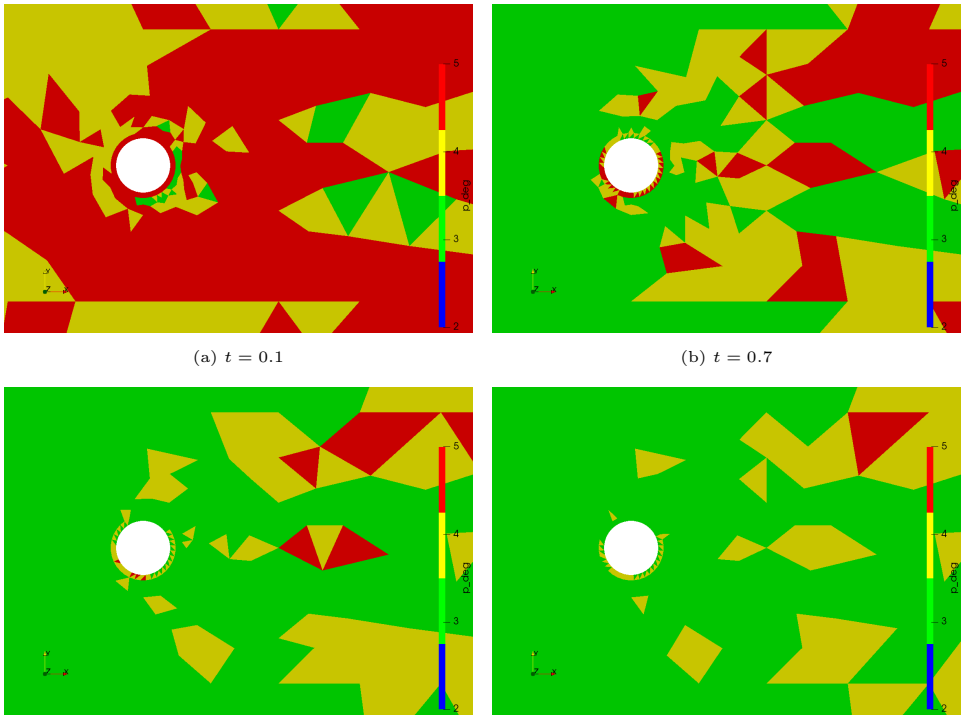

(a) $t = 0.1$

(b) $t = 0.7$

(c) $t = 0.9$

(d) $t = 1.1$

Figure 5.13: Polynomial distribution for the adaptive simulation $k = 2$ to 5

5.1.2 $Re = 1000$, $St_f = 0.6$

Once the $Re = 100$ experiments were completed, simulations with $Re = 1000$ were carried out, increasing the forcing frequency to 0.6. According to [16], the aforementioned pair of Re and St_f also resulted in vortex shedding synchronization. The same mesh 2 was initially used to serve as a benchmark to determine whether or not the current number of elements was sufficient to model the new flow configuration correctly. The values for the constant degree simulations are reported in Table 5.5. Convergence of the force statistics appears evident; however, Figures 5.15 and 5.14 indicate that mesh 2 is not properly capturing the physics. A finer mesh was then constructed with the same dimensions to obtain closer values to [16] and smoother visualizations.

$Mesh$	k	$DOFs$	Δr_b	$\Delta\theta_b$	C_l'	$\overline{C_d}$	St_{vs}
	2	7104	0.050	5.00°	0.251	0.585	0.6
2	3	11840	0.033	3.33°	0.193	0.612	0.6
	4	17760	0.025	2.50°	0.250	0.631	0.6
	5	24864	0.020	2.00°	0.232	0.640	0.6
	2	11568	0.0250	4.50°	0.218	0.635	0.6
2-Fine	3	19280	0.0167	3.00°	0.236	0.641	0.6
	4	28920	0.0125	2.25°	0.232	0.636	0.6
	5	40488	0.0100	1.80°	0.232	0.635	0.6

Table 5.5: Values for $Re = 1000$ and $St_f = 0.6$ for various polynomial degrees

Moving from degree 2 to 5 showed improvement on the values of the statistics signaling that degree refinement was necessary for both meshes. Although, it can be observed that the finer mesh reached statistical convergence more quickly than the coarse one.

The errors comparing the degree 5 values for each mesh to [16] are listed in Table 5.6. The drag is deemed sufficiently accurate, but the lift error is still rather high. This is attributed to insufficient resolution in the wake region even with the finer mesh.

	$C_{l_{err}}'$	$\overline{C_{d}}_{err}$	$St_{f_{err}}$
2	15.4%	4.3%	0.0%
2-Fine	15.4%	3.6%	0.0%

Table 5.6: Error values for constant $k = 5$ Simulations, $Re = 1000$, $St_f = 0.6$

Figure 5.14 plots the coefficient of drag versus the coefficient of lift for mesh 2. Here, it can be observed the effect of poor resolution in the wake. Despite the Reynolds number being increased by a factor of 10, the flow is still laminar, and one would expect something similar to the $Re = 100$ case. Instead, the quadratic elements clearly do not accurately simulate the flow. As the degree increases, the orbitals shift leftwards even passing through a supposedly correct solution with $k = 4$. Degree 5 begins to resemble Figure 5.4b, but remains asymmetric. This signals either degree 6 polynomials are necessary, or a finer grid. As stated previously, a finer grid was chosen.

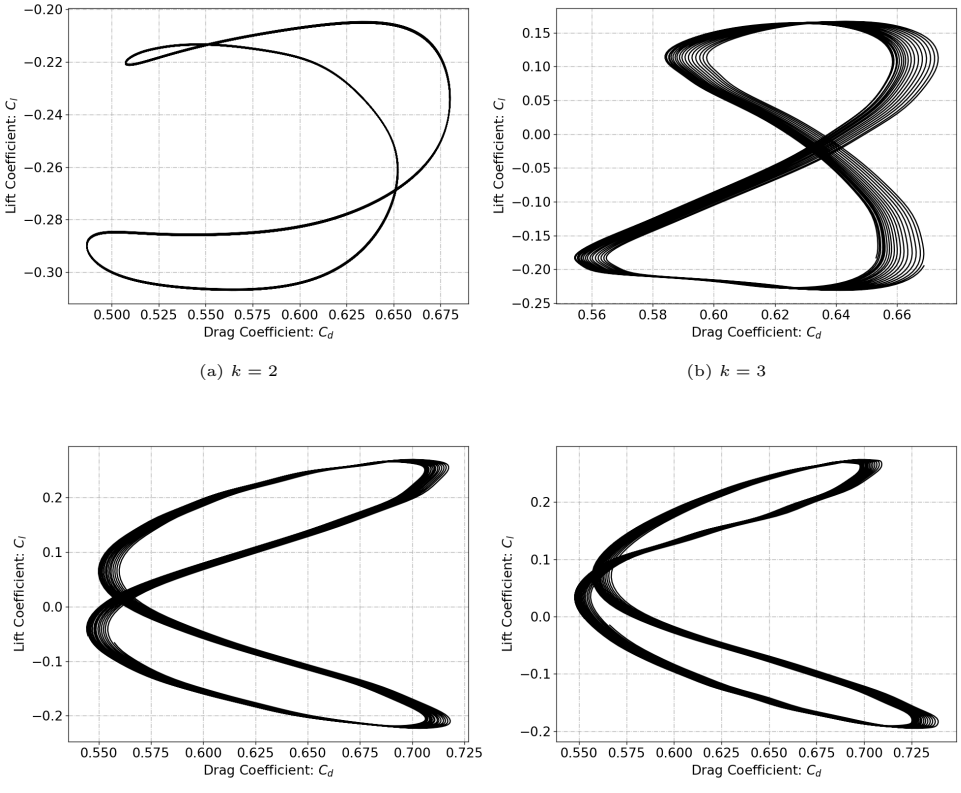

(a) $k = 2$

(b) $k = 3$

(c) $k = 4$

(d) $k = 5$

Figure 5.14: C_d vs. C_l Orbits for mesh 2: $Re = 1000$ and $St_f = 0.6$

Figure 5.15 compares the vorticity contours between mesh 2 and mesh 2-Fine. It is clear that the finer mesh was able to resolve the trailing vortices more precisely. To ensure that statistical convergence was reached for mesh 2-Fine, the coefficient of lift was once again plotted against the coefficient of drag. The updated orbital graph is shown in Figure 5.16. Notice that

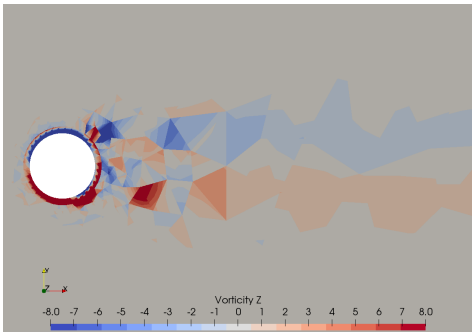

(a) $2 - Coarse$

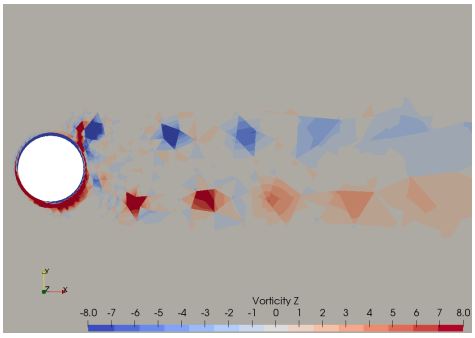

(b) $2 - Fine$

Figure 5.15: Vorticity contours comparing coarse vs. fine meshes at $Re = 1000$ for $k = 2$ simulations

the upper and lower lobes are now symmetrical and have a similar profile to the $Re = 100$ case. Thus, only the results of mesh 2-fine and degree 5 are presented since the force statistics and visualizations were the closest to that of [16].

The time history of the lift and drag are plotted in Figure 5.17. Both the force coefficients have reached a quasi-steady-state oscillating around a constant mean.

The force coefficients were calculated again with a time step of 0.01 as it proved to be sufficient in the $Re = 100$ case. Figure 5.18 displays the lift power spectrum for the $k = 2$ simulation. The peak amplitude is well depicted and matches the forcing one.

Figure 5.19 displays the vorticity contours at various time intervals. Recall the plots have been scaled to allow a better visualization of the shedding vortices. The vortices shed in couples and leave a trail in between the two vortex regions above and below the cylinder, unlike in the $Re = 100$ case. There exists a dominant vortex that travels downstream while the secondary vortex dissipates. The vortices again coalesce into a more traditional Von Kármán vortex street but notice that in this case the merging occurs closer

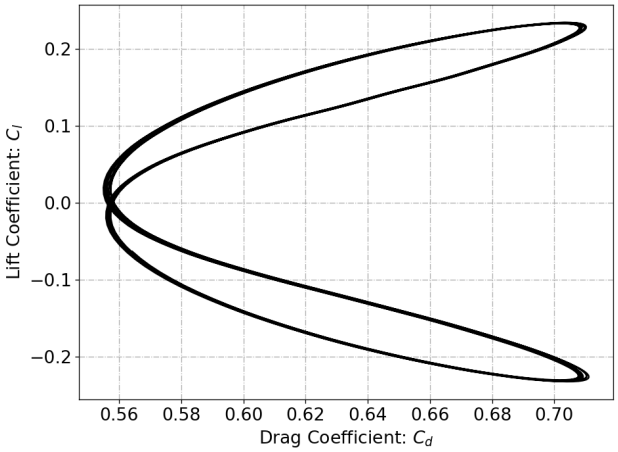

Figure 5.16: C_d vs. C_l Orbit: $Re = 1000$, and $St_f = 0.6$

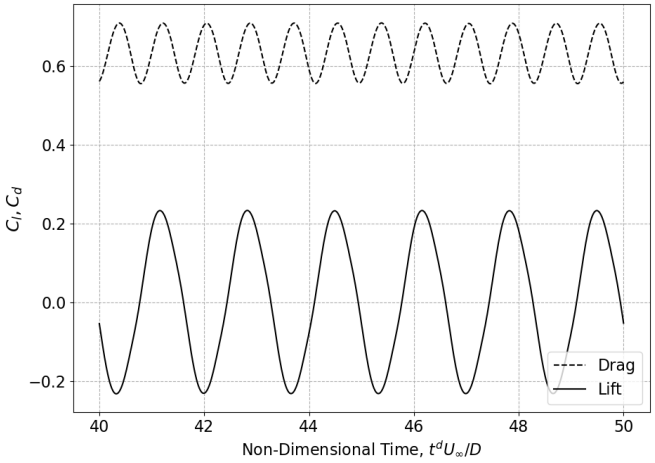

Figure 5.17: Time history of lift and drag coefficients: $Re = 1000$, and $St_f = 0.6$

to the cylinder (see Figure 5.20).

Since the values in Table 5.5 and Figure 5.15 varied more significantly than the $Re = 100$ case, a p-adaptive simulation was carried out once again. The RW Modal indicator was re-calculated and new time intervals were defined. For $Re = 1000$, a Δt_a of 0.033 was chosen since now the trailing vortices shed at a rate of 0.6 (corresponding to a period of 1.667 time units). Δt_i was adjusted to 10^{-3} to maintain a sufficient amount of values for averaging. Figure 5.21 shows the values of the indicator for one adaptation step and degree 4. The global time step remained unchanged to maintain

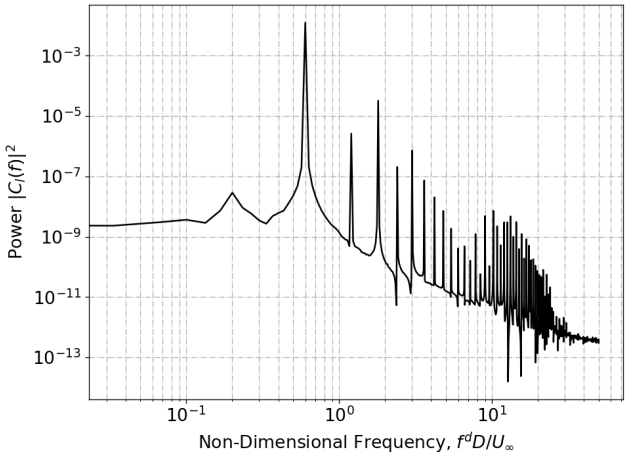

Figure 5.18: Power Lift Spectrum: $Re = 1000$, and $St_f = 0.6$

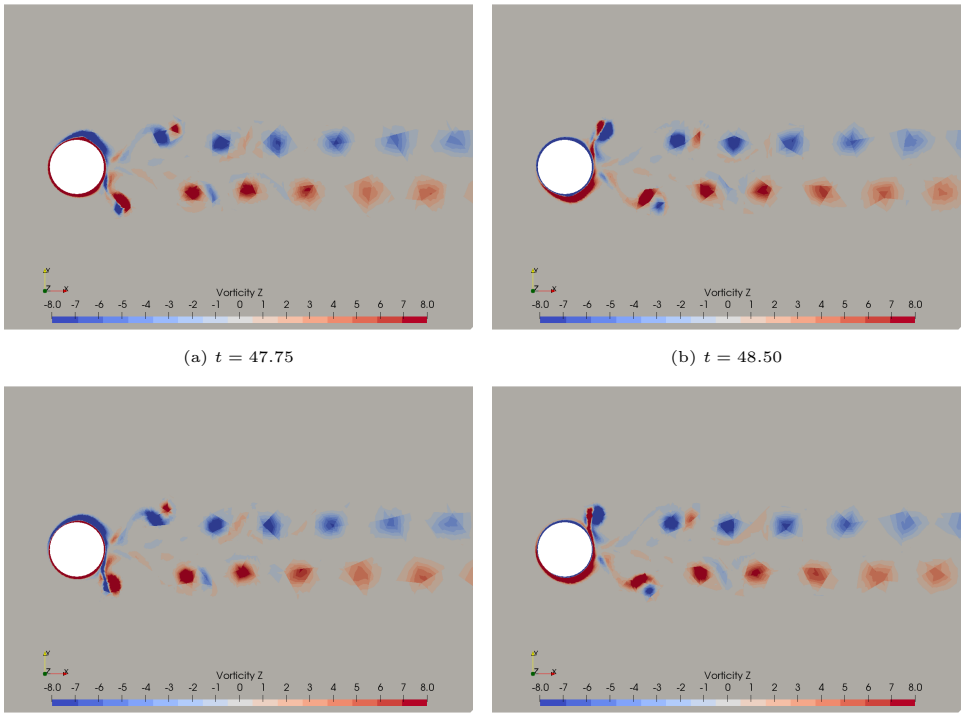

(a) $t = 47.75$

(b) $t = 48.50$

(c) $t = 49.25$

(d) $t = 50.0$

Figure 5.19: Vorticity contours for degree 5: $Re = 1000$ and $St_f = 0.6$

stability of the explicit time integration.

Notice that Figure 5.21 resembles Figure 6 in [59]. The RW Modal indicator is signaling for degree refinement in a more concentrated region

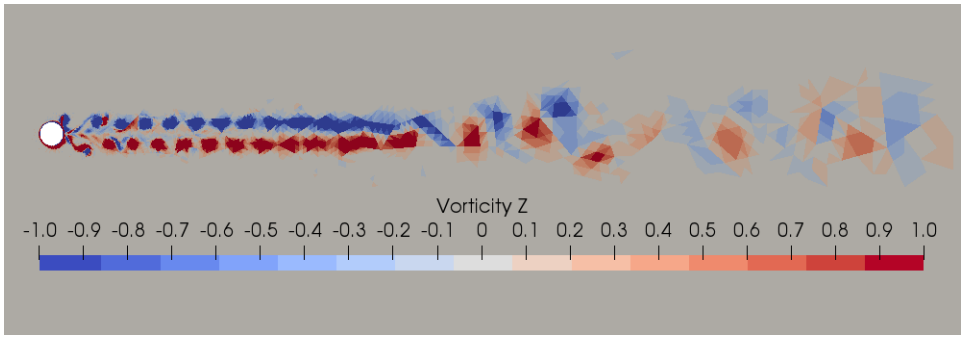

Figure 5.20: Cylinder wake: $Re = 1000$ and $St_f = 0.4$

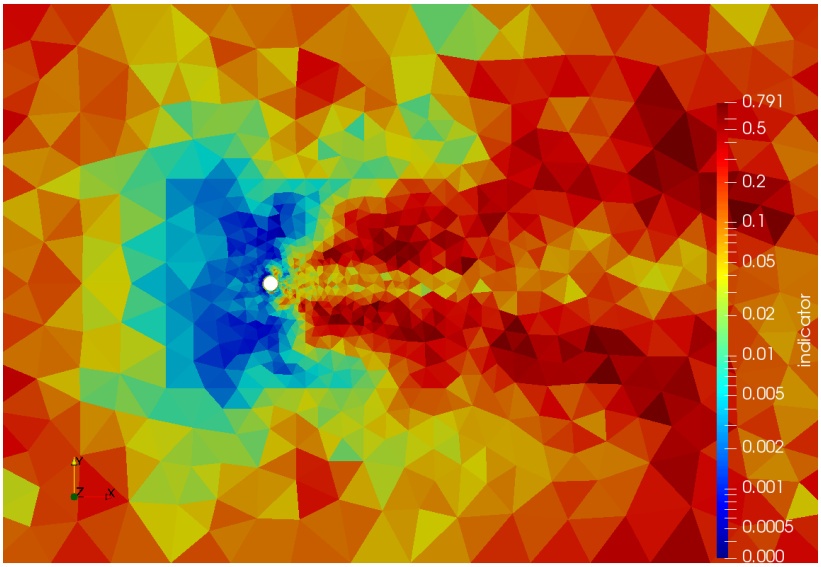

Figure 5.21: Logarithmic contour plot of the RW Modal Indicator for $k = 4$, $Re = 1000$, and $St_f = 0.6$

within the wake. Based on these preliminary calculations, the thresholds employed in the adaptive simulation are as follows: $\epsilon_1 = 0.01$, $\epsilon_2 = 0.08$, and $\epsilon_3 = 0.125$. These values resulted in a total amount of degrees of freedom of around 28400, roughly equivalent to the $k = 4$ case.

The simulation was initialized on the $k = 2$ solution and run for another 50 time units to ensure statistical convergence. Table 5.7 reports the values of force coefficients along with the Strouhal number for the adaptive simulation compared to the constant $k = 5$ degree. Notice how the resulting values agree well with the constant degree simulations while reducing the average time to compute one time step, $\bar{t}_{step}$, by 34.1%.

Figure 5.22 shows the polynomial distribution at the last time step. The

	$DOFs$	C_l'	$\overline{C_d}$	St_{vs}	$\bar{t}_{step}$
$k = 5$	40488	0.232	0.635	0.6	$0.675s$
$k = 2$ To 5	28400	0.235	0.635	0.6	$0.445s$

Table 5.7: Values for the adaptive simulation: $Re = 1000$, and $St_f = 0.6$ for $k = 2$ to 5

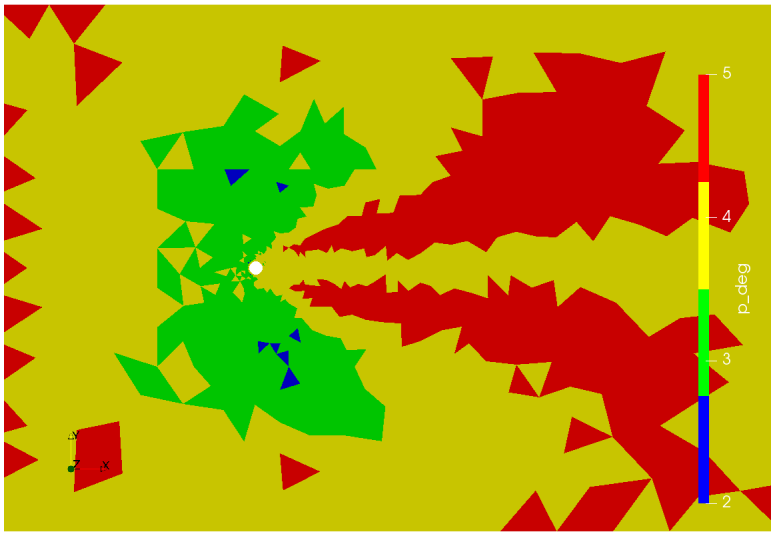

Figure 5.22: Adaptation step $t = 50.0$

chosen threshold range was selected to maintain at least degree 4 polynomials in the majority of the wake. The lower degree experiments did not yield satisfying results and the number of elements with polynomial order 2 and 3 was minimized for the adaptive simulation. Figure 5.23 zooms in on the cylinder to visualize the first few adaptation steps.

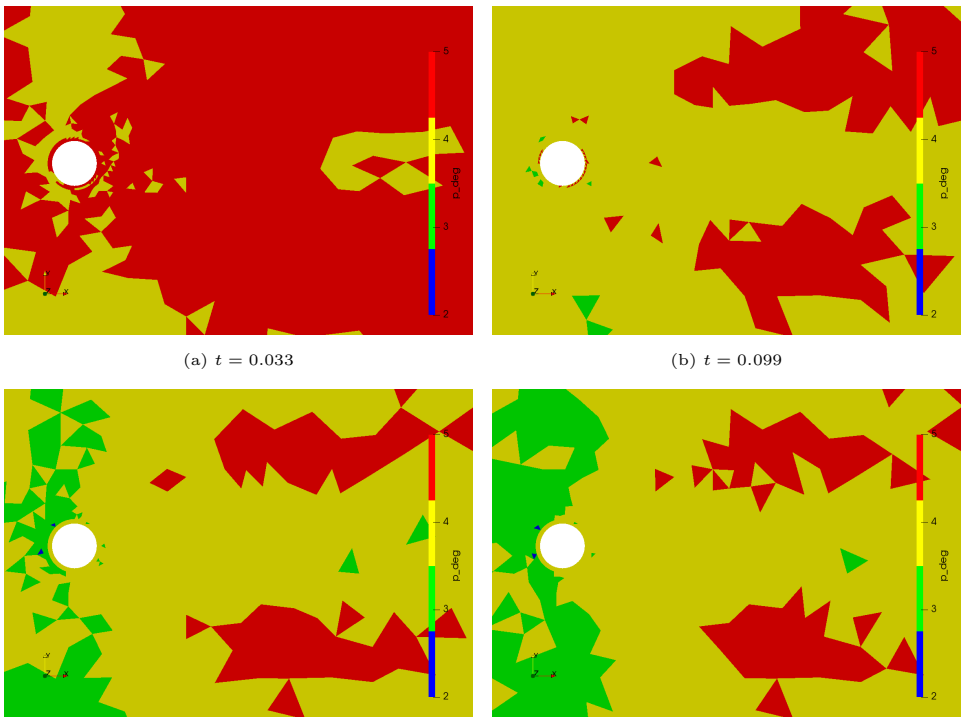

(a) $t = 0.033$ (b) $t = 0.099$

(c) $t = 0.132$ (d) $t = 0.198$

Figure 5.23: Polynomial distribution for the adaptive simulation: $Re = 1000$, $St_f = 0.6$ and $k = 2$ to $k = 5$

5.2 3D Turbulent Simulations with Constant Rotation

The turbulent test case simulated was that of flow past a cylinder with a constant rotational speed in a rotating reference frame. This configuration caused some issues that will be discussed in further detail in Appendix A.1. Despite these problems, meaningful results were obtained and are included here.

For this test case, the Reynolds number was set to 5000 and the non-dimensional rotation rate was fixed at 1 to match the experiments of Aljure *et al* in [6]. The cylinder remains the same dimension as in the 2D case ($D = 1$, $R_i = 0.5$). An O-grid was used with an outer radius of $12R_i$ and a thickness of $4R_i$ in the spanwise direction. The mesh can be seen in Figure 5.24.

To understand better the influence of turbulence, a simulation was first run using no LES models. Then, for comparison, the Anisotropic model was used due to it solving some of the main disadvantages of the Smagorinsky and Dynamic Models while costing a minimal number of additional computations.

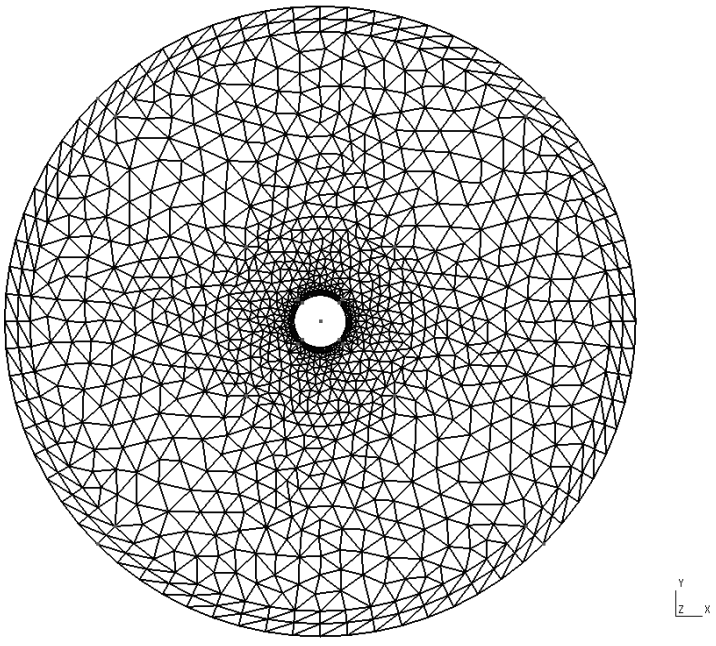

Figure 5.24: Mesh for 3D turbulent simulations

The *No* model simulation was run from $t = 0.0$ to 20.0 while the Anisotropic

model continued up to 30 non-dimensional time units. The mean values of the lift and drag coefficients from the last 10 time units of each case are reported in Table 5.8. A polynomial degree of 3 was chosen to obtain preliminary results and observe the behavior of the flow and the force statistics.

	k	Δr_b	$\Delta\theta_b$	$\overline{C_l}$	$\overline{C_d}$	St_{vs}
No Model	3	0.0671	2.727°	1.535	0.4507	0.43
Anisotropic	3	0.0671	2.727°	1.412	0.346	0.20

Table 5.8: Tabled Values for $\Omega = 1$ and $Re = 5000$

The lift coefficient matches well with [6]; however, the drag is still quite off. This is attributed to the poor initial resolution on the surface of the cylinder.

Figures 5.25 shows the time evolution of the two force coefficients. The time has been cut to remove the effects of the solution initialization.

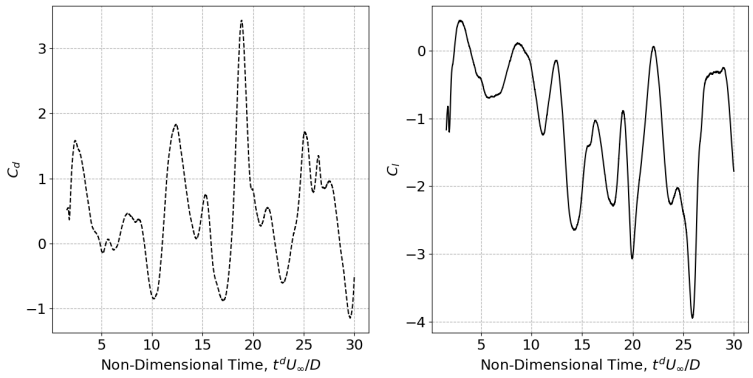

Figure 5.25: Lift and Drag Coefficient Time History

In addition, the mean force coefficients at every time step are also plotted to serve as an indicator of time convergence. It can be seen in Figure 5.26 that the force coefficients are not quite steady and still time dependent. Ideally, the simulation would continue to a longer time with more elements around the cylinder.

Unlike the 2D case, the 3D turbulent simulation was not run for sufficient time to clearly depict peaks in the frequency domain. To find the Strouhal number, a Butterworth band pass filter was applied to remove high frequency noise from the data [70]. Isolating the peak frequency of the filtered data yields a Strouhal number of 0.2. Comparing to the results of [6] (0.223) produces an error of 9.5%.

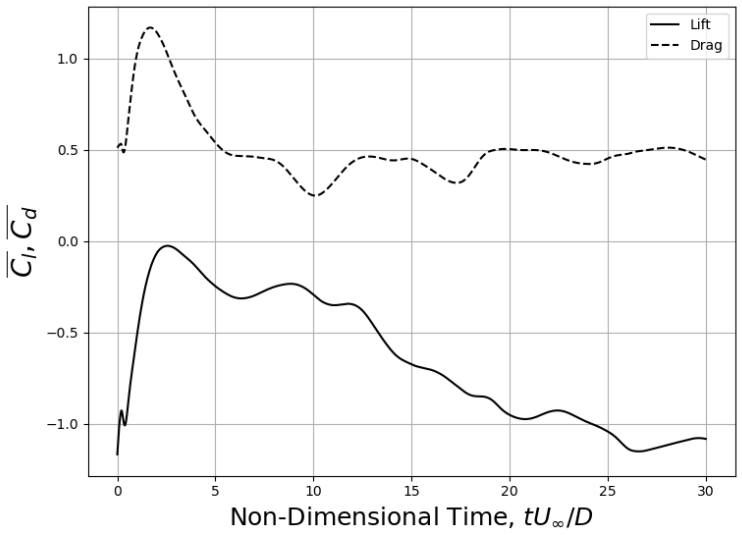

Figure 5.26: Mean Force Coefficients Development in Time, $\Omega = 1$, $Re = 5000$

For turbulent simulations, it is crucial to capture the laminar region within the boundary layer. Even at high Reynolds number, the viscous forces still dominate near the surface of the cylinder [42], [63]. An indicator to determine if the laminar region is properly resolved is the non-dimensional wall distance or y^+. This y^+ is similar to the one previous defined in Chapter 3 Section 3.2. However, now d^d_{wall} in Equation (3.23) refers to the position of the first node from the surface of the cylinder.

$$u^d_\tau = \sqrt{\frac{\tau^d_w}{\rho_r}} \tag{5.9}$$

is the wall friction velocity. Substituting (5.9) into (3.23) results in

$$y^+ = \frac{\rho_r d^d_{wall}}{\mu_r}\sqrt{\frac{\tau^d_w}{\rho_r}}. \tag{5.10}$$

It is convenient to use non-dimensional values to express y^+. If the freestream velocity is introduced, Equation (5.10) becomes

$$y^+ = \frac{\rho_r U_\infty d^d_{wall}}{\mu_r}\sqrt{\frac{\tau^d_w}{\rho_r U^2_\infty}}. \tag{5.11}$$

Notice that the term outside the radical is a local Reynolds number. To transform this into the global one used in the non-dimensional Navier-Stokes equations, the dimensional wall distance is normalized with respect to the cylinder diameter:

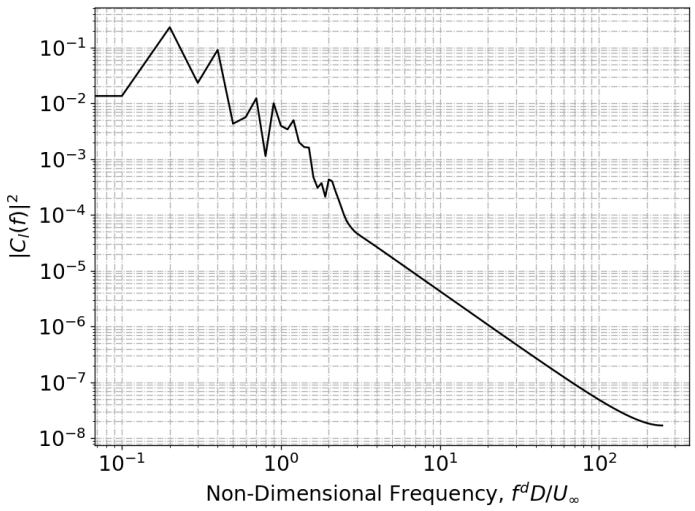

Figure 5.27: Lift Power Spectrum, $\Omega = 1$, $Re = 5000$

$$y^+ = \frac{d^d_{wall}}{D} Re \sqrt{\frac{\tau^d_w}{\rho_r U^2_\infty}}. \tag{5.12}$$

In regions where laminar separation occurs, the wall shear stress will become negative; therefore, the absolute value of $|\tau^d_w|$ is taken to ensure y^+ is always well defined.

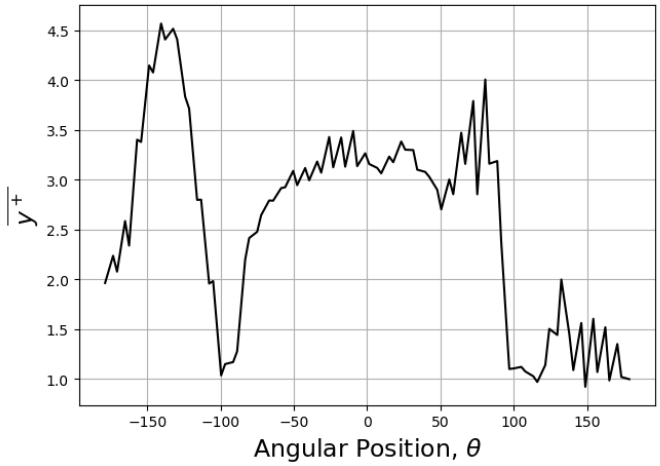

Figure 5.28: Non-dimensional Wall Distance y^+, $\Omega = 1$ and $Re = 5000$

Figure 5.28 plots y^+ along the circumference of the cylinder. The an-

gular position is measured going in the counterclockwise direction from the horizontal. Due to the transient nature of the flow, the y^+ values are averaged in time again for the last 10 time units of the simulation. The max and minimum values are reported in Table 5.9

	y^+_{min}	y^+_{max}
No Model	0.48	7.86
Anisotropic	0.92	4.57

Table 5.9: Min and Max Non-Dimensional Wall Distance for $\Omega = 1$ and $Re = 5000$

In practice y^+ should be in the range of at least 11.63 for proper capture of the viscous sublayer [63]. Note that, even though both the no model and Anisotropic model results are within this range, the resolution is suboptimal. Comparing Figure 5.28 with the one plotted by Cheng, Pullin, and Samtaney in [14], highlights the importance of having an adequate number of points along the surface of the boundary. The small local oscillations in Figure 5.28 are another indication that more simulation time and finer grid spacing were required to obtain more accurate results, despite the use of 3rd order polynomials.

Chapter 6

Concluding Remarks

Simulations of flow past a rotating cylinder were used to assess the capability of high order DG methods to produce sufficiently accurate results with time dependent boundary conditions. Both the constant degree and adaptive simulations had fewer degrees of freedom with respect to the reference simulations in [16]. Vortex shedding synchronization was obtained in the forced rotary oscillation test cases and the errors in the lift and drag coefficient were below 10% of the values reported in literature. A preliminary turbulent simulation in a non-inertial reference frame was also carried out. It was discovered that large computational domains are necessary to avoid boundary-object interactions. The additional forcing terms often caused undesirable or unrealistic results. Damping layers were used to smooth the solution to the prescribe boundary condition, but they had to be large to avoid any numerical instabilities related to velocity gradients.

For the laminar test cases, an analysis to determine the effectiveness of p-adaptivity was carried out. Due to the absence of the inter-element continuity restriction, the DG method is well suited for this study and yielded a significant reduction in computational time with respect to the constant degree simulations, without losing quality of the results. p-adaptivity is advantageous since no remeshing steps are carried out. As already seen in other experiments by Tugnoli *et al* in [59] and [5], initializing from a lower degree simulation produced sufficiently accurate results, while allowing to reduce substantially the cost of the complete simulation.

In the future, the hope is that p-adaptivity can be applied to rotating objects in a turbulent regime. Dynamic adaptivity will be employed since the numerical method will need to capture the transient nature of the convected eddies present in such a flow configuration. Additionally, dynamic load balancing is an interesting topic as it allows p-adaptivity to be even more efficient making use of multiple processors working simultaneously.

Appendix A

Simulations in a Non-Inertial Reference Frame

A.1 Potential Boundary Conditions Issues

Simulating flow past rotating objects often requires large computational domains to properly capture the wake. As discussed in Section 2.2, the centrifugal force increases with increasing radius. This causes the fluid to experience large forces. When solving the Navier-Stokes equations using a Galerkin approach, Dirichlet boundary conditions can be employed. This means there is the possibility that some nodes can be set to a value equal to 0. The sudden change in velocity can create numerical instabilities if not properly damped. The use of damping layers can reduce the impact of the centrifugal force however, they have to be wide enough to properly suppress unrealistic flow patterns.

While attempting to simulate flow past an oscillating rotating cylinder, vortices were observed being shed from the inlet since the fluid is traveling forward and experiencing a back and forth force in the non-inertial reference frame. These vortices would be reflected off the cylinder and cause spurious fluctuations. The various computed statistics were affected as a consequence and no longer represented the realistic flow development.

Although simulations in a non-inertial reference frame is not the focus of this thesis, the results of the conducted simulations are included in this appendix. The hope is that these results can be taken as advice for researchers attempting to simulate similar flow scenarios.

A.2 2D Flow Past a Cylinder with Non-Constant Rotation

As a numerical exercise, a simulation of the $\Omega = 2$, $St_f = 0.4$, and $Re = 100$ test case was performed using a rotating reference frame instead of applying a time dependent boundary condition. The velocity on the surface of the cylinder will now be equal to 0. The f_i term in Equation 2.18 is no longer null but contains the additional accelerations. Recall that in the derivation of Equation 2.18, the rotational velocity is the same for both observers. The same statement can be made for the oscillation frequency.

The boundary conditions on the outer domain, however, must be modified to account for the rotation. The inlet will change, and the freestream velocity will be calculated based on the position of the cylinder in time. In summary,

$$\begin{aligned} U_x &= U_\infty \sin(\Theta), \\ U_y &= U_\infty \cos(\Theta), \end{aligned} \tag{A.1}$$

where Θ is given by the integration of the oscillating rotation rate given by Equation 5.3 in Chapter 5.

$$\Theta = -\frac{\Omega}{2\pi St_f} \cos(2\pi St_f t) \tag{A.2}$$

The grid was changed to an O-type to better suite the physics of the problem similar to the one shown by Figure 5.24. Figure A.1 depicts the onset of the boundary vortex formation (only the vorticity magnitude is shown to magnify the phenomenon). The flow enters from the inlet and hits the cylinder. The wake begins to develop but after some time, a vortex forms at the boundary.

This boundary vortex is not physical and unfortunately was not properly handled in the initial 2D simulations. Ideally, these vortices would be suppressed by damping layers while still being near the boundaries or the domain would be large enough that they are convected away from the cylinder. The domain size is more important than in Chapter 5 Section 5.1 since the additional Coriolis and centrifugal terms are influencing the flow. Figure A.2 shows a boundary vortex interacting with the cylinder.

After these phenomena were observed, the decision to abandon simulating in a non-inertial reference frame was made. For the 3D turbulent case, the additional forcing terms had a lesser effect due to the constant rotation keeping the boundary vortices at a closer distance to the boundaries. Nevertheless, simulating in a rotating reference frame comes with its drawbacks and caution must be exerted.

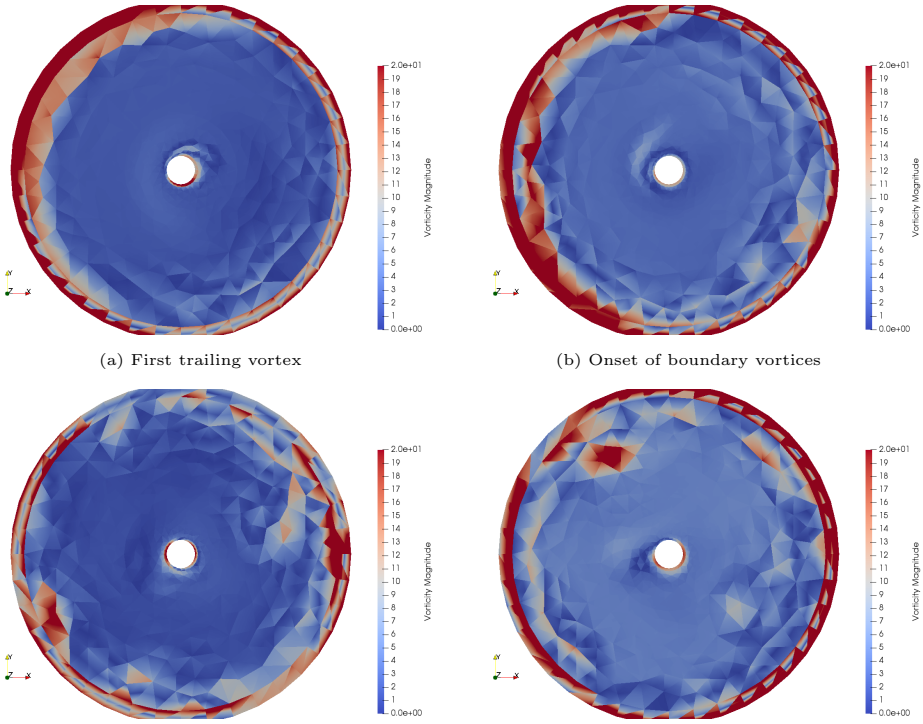

(a) First trailing vortex

(b) Onset of boundary vortices

(c) Boundary vortex beinging to form

(d) Boundary vortex formed

Figure A.1: Boundary vortex formation in a non-inertial reference frame

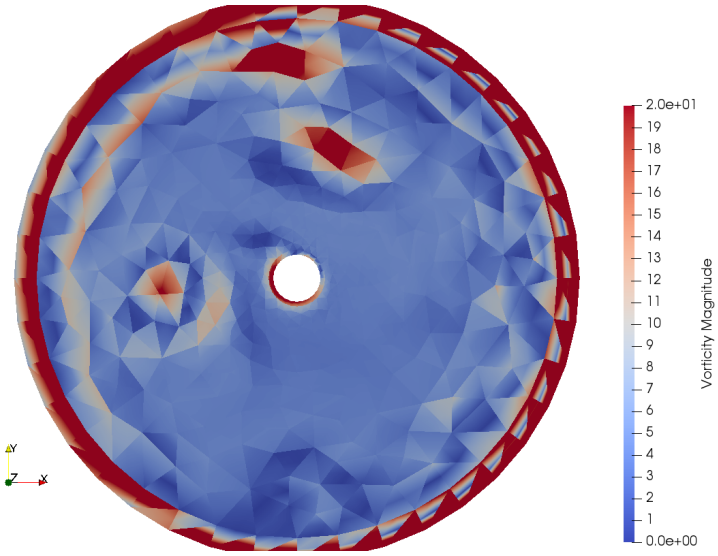

Figure A.2: Boundary vortex first contact with cylinder

Bibliography

[1] A. Abbà, L. Bonaventura, M. Nini, and M. Restelli. Dynamic models for Large Eddy Simulation of compressible flows with a high order DG method. *Computers & Fluids*, 122:209–222, 2015.

[2] A. Abbà, C. Cercignani, G. Picarella, and L. Valdettaro. A 3D Turbulent Boundary Layer Test for LES Models. In N. Satofuka, editor, *Computational Fluid Dynamics 2000*, pages 485–490, Berlin, Heidelberg, 2001. Springer Berlin Heidelberg.

[3] A. Abbà, C. Cercignani, and L. Valdettaro. Analysis of subgrid scale models. *Computers & Mathematics with Applications*, 46(4):521–535, 2003.

[4] A. Abbà, C. Cercignani, L. Valdettaro, and P. Zanini. LES of turbulent thermal convection. In *Proceedings from the Second ERCOFTAC Workshop on Direct and Large Eddy Simulation*, volume 5, 1997.

[5] A. Abbà, A. Recanati, M. Tugnoli, and L. Bonaventura. Dynamical p-adaptivity for LES of compressible flows in a high order DG framework. *Journal of Computational Physics*, 420:109720, 2020.

[6] D. E. Aljure, I. Rodríguez, O. Lehmkuhl, C. D. Pérez-Segarra, and A. Oliva. Influence of rotation on the flow over a cylinder at Re=5000. *International Journal of Heat and Fluid Flow*, 55:76–90, 2015.

[7] D. N. Arnold, F. Brezzi, B. Cockburn, and L. D. Marini. Unified Analysis of Discontinuous Galerkin Methods for Elliptic Problems. *SIAM Journal on Numerical Analysis*, 39(5):1749–1779, 2002.

[8] H. M. Badr, M. Coutanceau, S. C. R. Dennis, and C. Ménard. Unsteady flow past a rotating circular cylinder at Reynolds numbers 10^3 and 10^4. *Journal of Fluid Mechanics*, 220:459–484, 1990.

[9] F. Bassi and S. Rebay. A High-Order Accurate Discontinuous Finite Element Method for the Numerical Solution of the Compressible Navier–Stokes Equations. *Journal of Computational Physics*, 131(2):267–279, 1997.

[10] J. Boussinesq. *Essai sur la théorie des eaux courantes.* Mémoires présentés par divers savants à l'Académie des sciences de l'Institut national de France. Imprimerie Nationale, 1877.

[11] P. Castillo, B. Cockburn, I. Perugia, and D. Schötzau. An A Priori Error Analysis of the Local Discontinuous Galerkin Method for Elliptic Problems. *SIAM Journal on Numerical Analysis*, 38(5):1676–1706, 2000.

[12] C.-C. Chang and R.-L. Chern. Vortex shedding from an impulsively started rotating and translating circular cylinder. *Journal of Fluid Mechanics*, 233:265–298, 1991.

[13] J.-B. Chapelier, M. de la Llave Plata, F. Renac, and E. Lamballais. Evaluation of a high-order Discontinuous Galerkin method for the dns of turbulent flows. *Computers & Fluids*, 95:210–226, 2014.

[14] W. Cheng, D. I. Pullin, and R. Samtaney. Large-eddy simulation of flow over a rotating cylinder: the lift crisis at $Re_D = 6 \times 10^4$. *Journal of Fluid Mechanics*, 855:371–407, 2018.

[15] Y. Chew, M. Cheng, and S. Luo. A Numerical Study of Flow Past a Rotating Circular Cylinder Using a Hybrid Vortex Scheme. *Journal of Fluid Mechanics*, 299:35 – 71, 09 1995.

[16] S. Choi, H. Choi, and S. Kang. Characteristics of flow over a rotationally oscillating cylinder at low Reynolds number. *Physics of Fluids*, 14(8):2767–2777, 2002.

[17] M.-H. Chou. Numerical study of vortex shedding from a rotating cylinder immersed in a uniform flow field. *International Journal for Numerical Methods in Fluids*, 32(5):545–567, 2000.

[18] B. Cockburn, G. E. Karniadakis, and C.-W. Shu. *Discontinuous Galerkin Methods: Theory, Computation and Applications.* Springer Publishing Company, Incorporated, 1st edition, 2011.

[19] B. Cockburn and C.-W. Shu. The Local Discontinuous Galerkin Method for Time-Dependent Convection-Diffusion Systems. *SIAM Journal on Numerical Analysis*, 35(6):2440–2463, 1998.

[20] A. Cook. A Consistent Approach to Large Eddy Simulation Using Adaptive Mesh Refinement. *Journal of Computational Physics*, 154:117–133, 09 1999.

[21] M. Coutanceau and C. Ménard. Influence of rotation on the near-wake development behind an impulsively started circular cylinder. *Journal of Fluid Mechanics*, 158:399–446, 1985.

[22] J. W. Deardorff. A numerical study of three-dimensional turbulent channel flow at large Reynolds numbers. *Journal of Fluid Mechanics*, 41(2):453–480, 1970.

[23] T. M. Eidson. Numerical simulation of the turbulent Rayleigh–Bénard problem using subgrid modelling. *Journal of Fluid Mechanics*, 158:245–268, 1985.

[24] G. Erlebacher, M. Hussaini, C. Speziale, and T. Zang. Toward the Large Eddy Simulation of Compressible Turbulent Flows. 04 1987.

[25] C. Eskilsson. An hp-adaptive discontinuous Galerkin method for shallow water flows. *International Journal for Numerical Methods in Fluids*, 67:1605 – 1623, 12 2011.

[26] D. Flad, A. Beck, and C.-D. Munz. Simulation of underresolved turbulent flows by adaptive filtering using the high order discontinuous galerkin spectral element method. *Journal of Computational Physics*, 313:1–12, 2016.

[27] M. Germano. Turbulence: the filtering approach. *Journal of Fluid Mechanics*, 238:325–336, 1992.

[28] M. Germano, U. Piomelli, P. Moin, and W. H. Cabot. A dynamic subgrid-scale eddy viscosity model. In *Studying Turbulence Using Numerical Simulation Databases. 3: Proceedings of the 1990 Summer Program*, pages 5–17, 1990.

[29] C. Geuzaine and J.-F. Remacle. Gmsh: A 3-D finite element mesh generator with built-in pre- and post-processing facilities. *International Journal for Numerical Methods in Engineering*, 79(11):1309–1331, 2009.

[30] G. Gibertini, A. Abbà, F. Auteri, and M. Belan. Flow Around Two In-Tandem Flat Plates: Measurements and Computations Comparison. In *5th International Conference on Vortex Flows and Vortex Models (ICVFM2010)*, 2010.

[31] F. X. Giraldo. *A Space Marching Adaptive Remeshing Technique Applied to the 3D Euler Equations for Supersonic Flow*. PhD thesis, University of Virginia, 1995.

[32] F. X. Giraldo and M. Restelli. A study of spectral element and Discontinuous Galerkin methods for the Navier–Stokes equations in nonhydrostatic mesoscale atmospheric modeling: Equation sets and test cases. *Journal of Computational Physics*, 227(8):3849–3877, 2008.

[33] M. B. Glauert. The Flow Past a Rapidly Rotating Circular Cylinder. *Proceedings of the Royal Society of London Series A*, 242(1228):108–115, October 1957.

[34] G. Karypis and V. Kumar. A Fast and High Quality Multilevel Scheme for Partitioning Irregular Graphs. *SIAM J. Sci. Comput.*, 20(1):359–392, December 1998.

[35] D. Knight, G. Zhou, N. Okong'o, and V. Shukla. *Compressible large eddy simulation using unstructured grids*. 2000.

[36] A. N. Kolmogorov. The local structure of turbulence in incompressible viscous fluid for very large reynolds numbers. *Proceedings: Mathematical and Physical Sciences*, 434(1890):9–13, 1991.

[37] D. K. Lilly. The representation of small-scale turbulence in numerical simulation experiments. In *IBM Scientific Computing Symposium on Environmental Sciences*, 1966.

[38] D. K. Lilly. A proposed modification of the Germano subgrid-scale closure method. *Physics of Fluids A: Fluid Dynamics*, 4(3):633–635, 1992.

[39] X.-Y. Lu and J. Sato. A Numerical Study of Flow Past a Rotationally Oscillating Circular Cylinder. *Journal of Fluids and Structures*, 10(8):829–849, 1996.

[40] P. M. Martín, U. Piomelli, and G. V. Chandler. Subgrid-Scale Models for Compressible Large-Eddy Simulations. *Theoretical Computational Fluid Dynamics*, 13:361–376, 2000.

[41] S. Mittal and B. Kumar. Flow past a rotating cylinder. *Journal of Fluid Mechanics*, 476:303–334, 2003.

[42] B. R. Munson, T. H. Okishii, W. W. Huebsch, and A. P Rothmayer. *Fundamentals of Fluid Mechanics*. John Wiley & Sons, 2013.

[43] J. Park, K. Kwon, and H. Choi. Numerical solutions of flow past a circular cylinder at Reynolds numbers up to 160. *KSME International Journal*, 12(6):1200–1205, 1998.

[44] L. Prandtl et al. The Magnus effect and windpowered ships. *Naturwissenschaften*, 13(6):93–108, 1925.

[45] W. H. Reed and T. R. Hill. Triangular mesh methods for the neutron transport equation. In *National topical meeting on mathematical models and computational techniques for analysis of nuclear systems*, 10 1973. Report LA-UR-73-479.

[46] J.-F. Remacle, J. E. Flaherty, and M. S. Shephard. An Adaptive Discontinuous Galerkin Technique with an Orthogonal Basis Applied to Compressible Flow Problems. *SIAM Review*, 45(1):53–72, 2003.

[47] J.-F. Remacle, S. S. Frazão, X. Li, and M. S. Shephard. An adaptive discretization of shallow-water equations based on discontinuous Galerkin methods. *International Journal for Numerical Methods in Fluids*, 52(8):903–923, 2006.

[48] M. Restelli. Femilaro a finite element toolkit, 2016. Available at `https://bitbucket.org/mrestelli/femilaro/wiki/Home`.

[49] P. Sagaut. *Large Eddy Simulation for Incompressible Flows*. Springer, 2006.

[50] F. G. Schmitt. About Boussinesq's turbulent viscosity hypothesis: historical remarks and a direct evaluation of its validity. *Comptes Rendus Mécanique*, 335(9):617–627, 2007.

[51] U. Schumann. Subgrid scale model for finite difference simulations of turbulent flows in plane channels and annuli. *Journal of Computational Physics*, 18(4):376–404, 1975.

[52] A. Scotti, C. Meneveau, and D. K. Lilly. Generalized Smagorinsky model for anisotropic grids. *Physics of Fluids A: Fluid Dynamics*, 5(9):2306–2308, 1993.

[53] J. Seifert. A review of the Magnus effect in aeronautics. *Progress in Aerospace Sciences*, 55:17–45, 2012.

[54] J. Smagorinsky. General Circulation Experiments with the Primitive Equations. *Monthly Weather Review*, 91(3):99, 1963.

[55] R. J. Spiteri and S. J. Ruuth. A New Class of Optimal High-Order Strong-Stability-Preserving Time Discretization Methods. *SIAM Journal on Numerical Analysis*, 40(2):469–491, 2003.

[56] S. Taneda. Visual Observations of the Flow past a Circular Cylinder Performing a Rotatory Oscillation. *Journal of the Physical Society of Japan*, 45(3):1038–1043, 1978.

[57] P. T. Tokumaru and P. E. Dimotakis. Rotary oscillation control of a cylinder wake. *Journal of Fluid Mechanics*, 224:77–90, 1991.

[58] P. T. Tokumaru and P. E. Dimotakis. The lift of a cylinder executing rotary motions in a uniform flow. *Journal of Fluid Mechanics*, 255:1–10, 1993.

[59] M. Tugnoli, A. Abbà, L. Bonaventura, and M. Restelli. A locally p-adaptive approach for Large Eddy Simulation of compressible flows in a DG framework. *Journal of Computational Physics*, 349:33–58, 2017.

[60] G. Tumolo and L. Bonaventura. A semi-implicit, semi-Lagrangian Discontinuous Galerkin framework for adaptive numerical weather prediction. *Quarterly Journal of the Royal Meteorological Society*, 141(692):2582–2601, 2015.

[61] G. Tumolo, L. Bonaventura, and M. Restelli. A semi-implicit, semi-Lagrangian, p-adaptive Discontinuous Galerkin method for the shallow water equations. *Journal of Computational Physics*, 232(1):46–67, 2013.

[62] F. van der Bos, J. J. W. van der Vegt, and B. J. Geurts. A multi-scale formulation for compressible turbulent flows suitable for general variational discretization techniques. *Computer Methods in Applied Mechanics and Engineering*, 196(29):2863–2875, 2007.

[63] H. K. Versteeg and W. Malalasekera. *An introduction to computational fluid dynamics - the finite volume method.* Addison-Wesley-Longman, 2 edition, 2007.

[64] B. Vreman, B. Geurts, and H. Kuerten. Subgrid-modelling in LES of compressible flow. *Applied Scientific Reseach*, 54:191–203, 1995.

[65] D. C. Wilcox. *Turbulence Modeling for CFD.* DCW Ind., 1993.

[66] Zhiyin Yang. Large-eddy simulation: Past, present and the future. *Chinese Journal of Aeronautics*, 28(1):11–24, 2015.

[67] O. C. Zienkiewicz, J. P. De S. R. Gago, and D. W. Kelly. The hierarchical concept in finite element analysis. *Computers & Structures*, 16(1):53–65, 1983.

[68] O. C. Zienkiewicz, R. L. Taylor, and J. Z. Zhu. Chapter 4 - Variational Forms and Finite Element Approximation: 1-D Problems. In O.C. Zienkiewicz, R.L. Taylor, and J.Z. Zhu, editors, *The Finite Element Method: its Basis and Fundamentals (Seventh Edition)*, pages 93–113. Butterworth-Heinemann, Oxford, seventh edition edition, 2013.

[69] O. C. Zienkiewicz and J. Z. Zhu. Adaptivity and mesh generation. *International Journal for Numerical Methods in Engineering*, 32(4):783–810, 1991.

[70] H. Zumbahlen. Chapter 8 - Analog Filters. In H. Zumbahlen, editor, *Linear Circuit Design Handbook*, pages 581–679. Newnes, Burlington, 2008.